# Compositional Variations in Sedimentary Deposits in Gale Crater as Observed by ChemCam Passive and Active Spectra

H. T. Manelski[1*], R. Y. Sheppard[2], A. A. Fraeman[3], R. C. Wiens[1], J. R. Johnson[4], E. B. Rampe[5], J. Frydenvang[6], N. L. Lanza[7], O. Gasnault[8]

[1]Earth, Atmospheric, and Planetary Sciences, Purdue University, West Lafayette, IN, USA
[2]Planetary Science Institute, Tucson, AZ, USA
[3]Jet Propulsion Laboratory, California Institute of Technology, Pasadena, CA, USA
[4]Applied Physics Laboratory, Johns Hopkins University, Laurel, MD, USA
[5]NASA Johnson Space Center, Houston, TX, USA
[6]University of Copenhagen, Copenhagen, Denmark,
[7]Los Alamos National Laboratory, Los Alamos, NM, USA
[8]Institut de Recherche en Astrophysique et Planétologie, Université de Toulouse 3, CNRS, CNES, Toulouse, France

*corresponding author: hmanelsk@purdue.edu

## Key Points:

- Principal component and spectral parameter analysis of ChemCam passive spectra highlight four spectral endmembers in Mt. Sharp group rocks
- A decrease in near-infrared slope is seen in the Hutton interval, suggesting a changing depositional environment or enhanced diagenesis
- Bedrock containing Mg-sulfates and Ca-sulfate cements are highlighted in a multivariate survey of ChemCam passive spectra

**Abstract**

During the first 2934 sols of the Curiosity rover's mission 33,468 passive visible/near-infrared reflectance spectra were taken of the surface by the mast-mounted ChemCam instrument on a range of target types. ChemCam spectra of bedrock targets from the Murray and Carolyn Shoemaker formations on Mt. Sharp were investigated using principal component analysis (PCA) and various spectral parameters including the band depth at 535 nm and the slope between 840 nm and 750 nm. Four endmember spectra were identified. Passive spectra were compared to Laser Induced Breakdown Spectroscopy (LIBS) data to search for correlations between spectral properties and elemental abundances. The correlation coefficient between $FeO_T$ reported by LIBS and BD535 from passive spectra was used to search for regions where iron may have been added to the bedrock through oxidation of ferrous-bearing fluids, but no correlations were found. Rocks in the Blunts Point-Sutton Island transition that have unique spectral properties compared to surrounding rocks, that is flat near-infrared (NIR) slopes and weak 535 nm absorptions, are associated with higher Mn and Mg in the LIBS spectra of bedrock. Additionally, calcium-sulfate cements, previously identified by Ca and S enrichments in the LIBS spectra of bedrock, were also shown to be associated with spectral trends seen in Blunts Point. A shift towards steeper near-infrared slope is seen in the Hutton interval, indicative of changing depositional conditions or increased diagenesis.

**Plain Language Summary**

The Chemistry and Camera (ChemCam) instrument on the Mars Science Laboratory Curiosity rover was built for use in 'active' mode: in which a laser vaporizes a small amount of material from a targets' surface and the light emitted from the resulting plasma is used to quantify the relative amounts of various elements. ChemCam also collects 'passive' spectra (without the use of the laser). These passive spectra use reflected sunlight to provide complementary mineralogical information. By looking at how passive and active spectral features relate and change we can further our understanding of the composition of targets that the rover has encountered. Comparison between passive spectral parameters and iron oxides reported by active spectroscopy identified two regions (Sutton Island to Blunts Point and Glasgow to Knockfarril Hill transitions) as areas of compositional interest and show evidence of variations in oxidation conditions. The passive spectra are also shown to be largely in agreement with data from CheMin, another instrument on Curiosity which provides mineralogical analysis of powdered samples.

## 1. Introduction

The Mars Science Laboratory's (MSL) Curiosity rover landed on the northern plains of Gale crater, a ~154 km diameter impact crater in southern Elysium Planitia, along the planetary dichotomy, in August of 2012. Since landing, Curiosity has travelled across the crater floor and then up the side of Mt. Sharp (formally known as Aeolis Mons) with a goal to characterize the past environments preserved in the region's sedimentary rock record, and to determine if these environments would have been habitable (Vasavada, 2022 and references therein).

Visible and near-infrared (VNIR, ~400-1000 nm) reflectance spectroscopy plays a key role in the suite of tools Curiosity uses to identify the composition of materials it encounters. This spectral range is sensitive to broad charge-transfer and crystal field absorptions that are most commonly associated with iron-bearing minerals (e.g. Wellington et al., 2017). Curiosity's Mast Camera

(Mastcam) measures relative reflectance of the surface from 400-1020 nm in up to 12 unique wavelengths (Bell et al., 2017; Malin et al., 2017). Multispectral observations have been demonstrated to discriminate compositionally distinct materials in Gale Crater, and they qualitatively agree with mineralogy from samples measured by Curiosity's X-ray diffraction instrument (Horgan et al., 2020; Jacob et al., 2020; Wellington et al., 2017). Large scale surveys of the VNIR spectral properties of rocks, soils, and veins along curiosity's traverse conducted using Mastcam data from sols 0-2302 have been interpreted to reveal nine rock spectral classes (Rice et al., 2022). The spectral differences between classes were understood to be caused predominantly by variations in grain size and abundance of hematite and other iron oxides (Rice et al., 2022). Rock spectral variability was also observed to align with stratigraphic members in some cases (Horgan et al., 2020; Rice et al., 2022).

Early in Curiosity's mission, a novel protocol was developed to calibrate passive radiance measurements from the Chemistry and Camera (ChemCam) (i.e., without the use of ChemCam's laser) to relative reflectance using well-characterized Mastcam and ChemCam calibration targets, creating a VNIR relative reflectance spectra dataset (Johnson, 2022; Johnson et al., 2015). In contrast to Mastcam, which is an imager, ChemCam collects point spectra from spots that are nanometers to micrometers in size. Like Mastcam spectra, ChemCam relative reflectance spectra proved useful in classifying material near Curiosity's landing site and observing airfall dust coverage and have been shown to be sensitive to mineralogy, with the ability to distinguish major Fe-bearing minerals (e.g., hematite and ferric sulfates) in Mt. Sharp, sometimes as far away as several kilometers (Johnson et al., 2015, 2016). ChemCam passive spectra have also been demonstrated to be consistent with Chemistry and Mineralogy (CheMin) X-ray diffraction data (Johnson et al., 2016; Wellington et al., 2017).

In active mode, ChemCam uses laser ablation in the form of laser induced breakdown spectroscopy (LIBS) to investigate rocks and regolith in Gale Crater (Maurice et al., 2012; Wiens et al., 2012). LIBS provides information about the elemental composition of geologic materials and is especially valuable because it can be used to investigate targets several meters away, removes most of the airfall dust from the observation area (Graff et al., 2011; Johnson et al., 2015), and has the ability to sense chemical changes with depth (Lanza et al., 2012). ChemCam acquires a passive spectrum before and/or after each LIBS observation, so almost all the passive reflectance spectra pair one-to-one with a LIBS elemental abundance measurement. The correlated LIBS elemental chemistry and passive spectral datasets therefore provide a unique resource to track how the reflectance properties and chemical composition varied over the course of the traverse at the nanometer to micrometer scale.

This paper expands upon and complements previous investigations of ChemCam passive and Mastcam spectral data of rocks in the lower portion of Mt. Sharp (Fraeman et al., 2020; Haber et al., 2022; Horgan et al., 2020; Jacob et al., 2020; Johnson et al., 2015, 2016; Rice et al., 2022; Wellington et al., 2017). Here, the spectral properties of bedrock targets in Mt. Sharp's Murray and Carolyn Shoemaker formations observed by ChemCam passive spectra are studied using principal component analysis (PCA) along with band depth and spectral slope/ratio calculations. This spectral dataset comprises a subset of 9,400 passive spectra acquired between sols 776 and 2934 of Curiosity's mission. This work also for the first time investigates paired ChemCam LIBS elemental composition data and passive reflectance spectra with the goal to investigate the

source(s) and implications of spectral trends seen in the ChemCam passive data set. Where available, ChemCam data are also compared with mineralogy reported by the Chemistry and Mineralogy (CheMin) instrument to search for further insight into sources of spectral variability.

## 2. Background

### 2.1 Mount Sharp Geology

Gale crater is a ~3.7-billion-year-old impact feature near the boundary of the northern highlands and southern lowlands of Mars (e.g., Pelkey & Jakosky, 2002). Gale crater contains a central mound, Mount Sharp, that rises ~5.5 km above the surrounding terrain (e.g., Thomson et al., 2011) and provides an unprecedented opportunity to examine hundreds of meters of stratigraphy that may preserve clues to the past climate history and habitability of Mars.

The sedimentary rocks that Curiosity has traversed can be divided into three geologic groups: (1) the Bradbury group, where Curiosity landed and explored for the first 776 sols of its mission, is composed of diverse sedimentary units including fluvial, aeolian, and lacustrine deposits along the crater floor; (2) the Mount Sharp group, which is the sedimentary group that makes up the primary structure of Mount Sharp; and (3) the Siccar Point group, which unconformably overlies the Mount Sharp group and is composed of younger aeolian sandstone deposits (Vasavada, 2022). This paper will focus on the Mount Sharp group prior to sol 2934.

The Mount Sharp group has been subdivided into several formations and members by the MSL Team (Fig. 1; Table 1). The Murray formation is ~300 m thick and is composed of the Pahrump Hills, Hartmann's Valley, Karasburg, Sutton Island, Blunts Point, Pettegrove Point, and Jura stratigraphic members. This formation was predominantly deposited in lacustrine and marginal lacustrine environments (Edgar et al., 2020; Gwizd et al., 2022; Stack et al., 2019). The ~70 m thick Carolyn Shoemaker formation sits above the Murray formation, and it subdivides into the Knockfarril Hill and Glasgow members. The Carolyn Shoemaker formation has an increased diversity of depositional environments compared to the Murray formation, including evidence for higher energy fluvial systems (Bennett et al., 2022; Caravaca et al., 2022; Vasavada, 2022, Fedo et al., 2022).

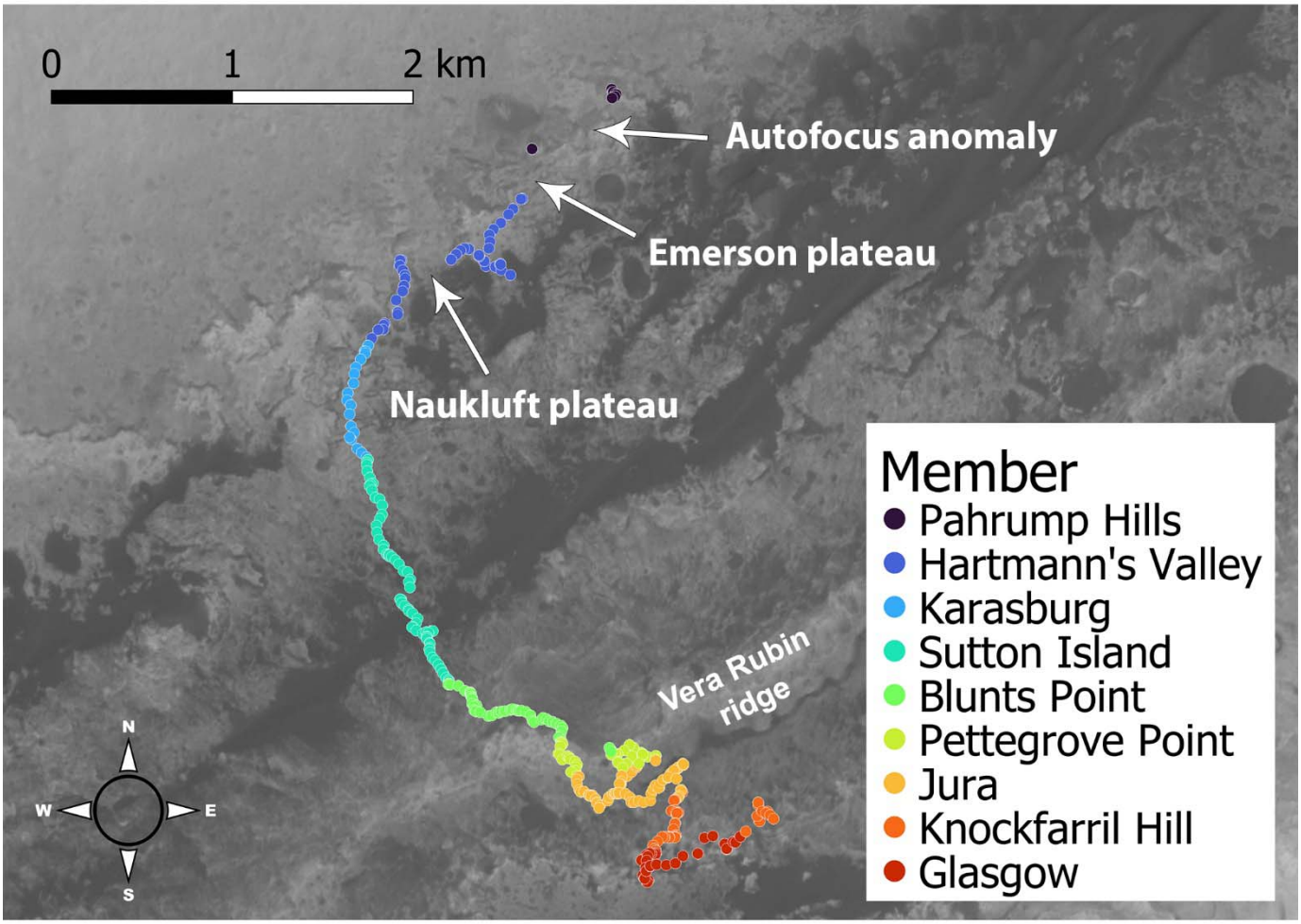


**Figure 1.** All ChemCam bedrock targets in the Murray and Carolyn Shoemaker formations, up to sol 2934, colored by stratigraphic member (Table 1). Gaps in the earlier part of the data are due to traversing aeolian strata at Emerson and Naukluft Plateaus, and to a temporary anomaly with ChemCam's autofocus. Knockfarril Hill and Glasgow are part of the Carolyn Shoemaker formation, all other members are part of the Murray Formation. The base map is a CTX 6 meter mosaic (Calef & Parker, 2016).

**Table 1.** Stratigraphic Members in the Mt. Sharp group

| Stratigraphic formation | Stratigraphic member | Approximate sol range | Elevation relative to MOLA datum (m) |
|---|---|---|---|
| Murray | Pahrump Hills | 776-797, 807-950, 997-1035, 1067-1072 | −4460 to −4437 |
| Murray | Hartmann's Valley | 1105-1108, 1154-1276, 1354-1412 | −4437 to −4412 |
| Murray | Karasburg | 1413-1473 | −4412 to −4375 |

| | | | |
|---|---|---|---|
| Murray | Sutton Island | 1474-1690 | −4375 to −4280 |
| Murray | Blunts Point | 1691-1809, 2046-2094 | −4280 to −4210 |
| Murray | Pettegrove Point | 1810-1873, 2000-2014, 2024-2045, 2095-2157, | −4210 to −4172 |
| Murray | Jura | 1874-1999, 2015-2023, 2158-2439, 2448-2453 | −4172 to −4143 |
| Carolyn Shoemaker | Knockfarril Hill | 2440-2447, 2454-2606, 2817-2950 | −4143 to −4117 |
| Carolyn Shoemaker | Glasgow | 2607-2695, 2735-2816 | −4117 to 4072 |

**Note.** Geological member/formation sol (Martian day) ranges and elevations (Edgar et al., 2020; Fedo et al., 2022; Gwizd et al., 2022; Stack et al., 2016)

### 2.2 Spectral Features

The wavelength range of ChemCam's passive spectral measurements is sensitive to electronic transitions, including charge transfer and crystal field splitting. Crystalline ferric oxides and oxyhydroxides including crystalline hematite have four characteristic broad electronic absorptions in this range: 400-415 nm, 485-550 nm, 650-710 nm, and 804-910 nm (Morris et al., 1985; Sherman et al., 1982; Sherman, 1985; Sherman & Waite, 1985). Poorly crystalline, nanophase Fe oxides lack these distinct spectral absorptions and are characterized by a steep spectral edge between 400-750 nm (Bell et al., 1990, 2000). Magnetite, a mixed-valence Fe oxide, has a relatively flat, low-reflectance spectrum with a local minimum near 550 nm and local maximum near 650 nm, caused by closely co-located $Fe^{2+}$ and $Fe^{3+}$ in both tetrahedral and octahedral coordination (Izawa et al., 2019). Although a variety of factors (e.g., particle size, opaque minerals) can influence the strength of an absorption band in reflectance spectra, calculating relevant band depth, band positions, and spectral slopes can provide a measurement of relative absorption strength between samples.

## 3. Methods

### 3.1 ChemCam Passive Spectral Data Acquisition and Treatment

ChemCam passive surface spectral data calibrated to relative reflectance using the methods described in Johnson et al., (2015, 2016) are available from NASA's Planetary Data System (PDS) Geosciences Node (Johnson, 2022). ChemCam uses three spectrometers to measure reflected radiance: the UV spectrometer (240.1-342.2 nm), violet (VIO) spectrometer (382.1-469.4 nm), and visible/near infrared (VNIR) spectrometer (474.0-906.5 nm) (Wiens et al., 2012). Passive spectra are restricted to 440-840 nm because the UV spectrometer responsivity, VIO spectrometer responsivity <440 nm, and VNIR spectrometer responsivity >840 nm are relatively low, resulting in low SNR in the passive reflectance spectra (Johnson et al., 2015). Data near the detector edges around the gap between the VIO and VNIR spectrometers, from ~469-474 nm, are also associated with low SNR due to low detector responsivity (Wiens et al., 2012). The trimmed spectra were passed through a Savitzky-Golay filter (SG) for smoothing, which fit subsets of nearby points with a cubic polynomial via linear least squares (Savitzky & Golay,

1964). This smoothing step ensured that spectral features were not a result of localized noise. Spectra that had at least one negative value for relative reflectance between 440-840 nm after filtering (256 spectra) were deemed invalid and removed from the dataset. Spectra were co-registered with orbital basemaps using QGIS, and MSL localizations from the sol the spectra were acquired were used to assign each measurement a latitude and longitude (Deen, 2015).

ChemCam surface reflectance passive spectra of each observation were manually classified by Johnson (2022) into target types such as bedrock, veins, calibration targets, soils, and sands. An example of 1x5 ChemCam raster target that covers vein, bedrock, and mixed vein and bedrock classified material is shown in Fig. 2. Of the 33,631 passive spectra taken in the first 2934 sols, 16,246 (48.3%) are solely categorized as bedrock targets. Only Murray and Carolyn Shoemaker formation targets classified as "bedrock" collected prior to sol 2934 were included in the analyses described below (9,400 observations). It is important to note LIBS measurements give information about a smaller radius of material due to the narrower size of the laser beam compared to the spectrometer IFOV (~400 µm for the laser spot size vs. ~1.3-2.6 mm for the ChemCam passive spectral for targets 2-4 m away; Maurice et al., 2012; Wiens et al., 2012), so their sampling areas are different.

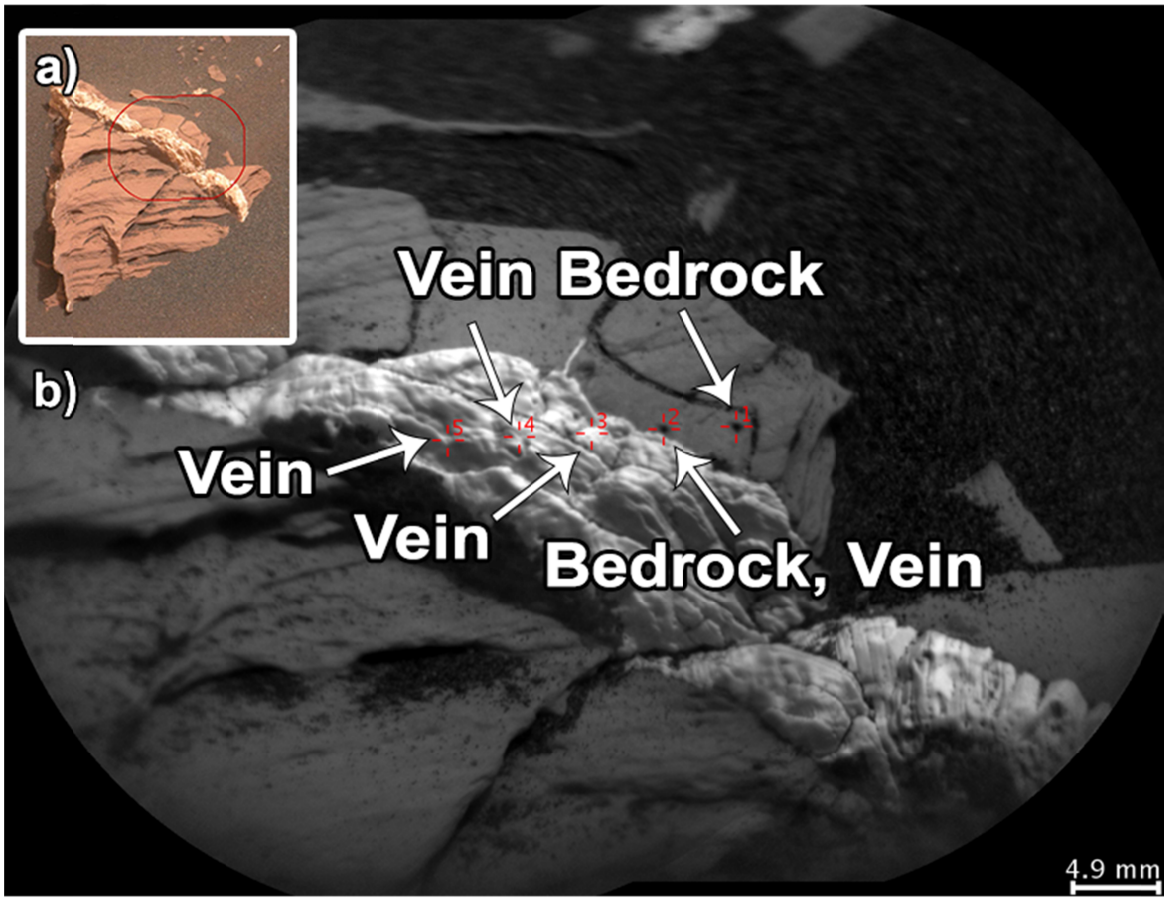


**Figure 2.** Example of different types of ChemCam target materials (target Tofte on sol 2080). (a) The red ellipse in this Mastcam mosaic context image shows the location of the RMI. (b) Each of the red crosshairs in this RMI image corresponds to a LIBS and passive spectral target. Target type classifications for each point are shown.

### 3.2 Spectral characterization

The shape and location of a spectral absorption, as well as the overall shape of the spectrum itself, can be described by numerical parameterizations such as band depths and spectral slopes. Previous studies have found several spectral parameters that are particularly effective for evaluating characteristics of ChemCam passive spectra, summarized in Table 2 (Johnson et al., 2015, 2016).

**Table 2.** Equations to Calculate Spectral Parameters (Fraeman et al., 2020; Johnson et al., 2015).

| Spectral parameter | Equation | Description |
|---|---|---|
| BD535 | $1 - \frac{R^*_{535}}{0.65R^*_{500} + 0.35R^*_{600}}$ | Positive when $Fe^{3+}$ is present |
| BD600 | $1 - \frac{R^*_{600}}{0.52R^*_{535} + 0.48R^*_{670}}$ | Related to the strength of the short wavelength ferric oxide absorption edge |
| R6744 | $\frac{R^*_{670}}{R^*_{440}}$ | VIS ratio, related to airfall dust coverage |
| R6084 | $\frac{R^*_{840}}{R^*_{600}}$ | NIR ratio |
| S7584 | $\frac{R^*_{840} - R^*_{750}}{(840 - 750)}$ | NIR slope, indicative of the strength of iron absorptions |
| Spectral Maximum | NA | Wavelength at which $R^*$ is highest. |
| Average relative reflectance | $\frac{\sum R^*}{2462}$ | Average relative reflectance of a target from 440 to 840 nm |

**Note.** $R^*_{\#\#\#}$ is the relative reflectance after smoothing with the Savitsky-Golay filter at ### nm. Average relative reflectance is the sum of the relative reflectance divided by the total number of channels between 440 and 840 nm (2462).

Two prominent spectral parameters used here were the band depth at 535 nm (BD535) and slope between 840 nm and 750 nm (S7584) (Table 2). The absorption at 535 nm is caused by the presence of ferric phases. The slope from 840-750 nm can be a proxy for a broad absorption feature centered at ~860 nm, which is related to some ferric phases such as hematite (Morris et al., 1985), although it can also be sensitive to the broad $Fe^{2+}$ absorption near 1000 nm associated with olivine and pyroxene. Combined, large BD535 and S7584 values have been confirmed to

provide evidence for the presence of ferric phases (Fraeman et al., 2020; Jacob et al., 2020; Wellington et al., 2017).

### 3.3 LIBS Elemental Abundance Data

ChemCam LIBS spectra were converted into major oxide compositions (MOC) via a calibration model that uses a weighted average of two multivariate approaches: partial least squares and independent component analysis (Clegg et al., 2017). This model was trained on a diverse set of 408 pressed power samples with independently measured compositions and cross validation was used to tune relevant modelling parameters. The result is MOC tables that report wt% of various oxides as well as corresponding Root Mean Squared Error of Prediction (RMSEP) values for all points analyzed by LIBS. These MOC tables are available from the PDS Geosciences Node (Wiens, 2022).

ChemCam acquires a passive spectrum before or after each LIBS observation, so almost all the passive spectra of bedrock in the Murray and Carolyn Shoemaker formations pair one-to-one with a LIBS elemental abundance measurement. The correlated LIBS elemental chemistry and passive spectral datasets allow for tracking how the spectral properties compare with chemical composition, and how both changed over the course of the traverse. Although data were acquired between sols 801 and 985, during the resolution of the ChemCam autofocus problem (Peret et al., 2016), the mode of observation during this period makes it more difficult to match LIBS and passive spectra, so this period was not considered in this study (Fig. 1).There is also a subset of "passive only" targets, where data were collected without LIBS (Johnson et al., 2015, 2016), and those targets are also not included in this work. All major oxides reported by ChemCam ($FeO_T$, MgO, $SiO_2$, CaO, $Na_2O$, $K_2O$, $TiO_2$, and $Al_2O_3$) were included in the analysis, as was MnO (Gasda et al., 2021). Iron abundances are given as FeO, regardless of the actual oxidation state, because the oxidation state is not determined by routine LIBS analysis.

### 3.4 Principal Component Analysis (PCA)

PCA is a dimensionality reduction technique which converts a n-dimensional data cloud into orthogonal principal components (PCs) sorted from high to low percentages of the variance in the dataset that can be summarized with only a few axes, to aid in analysis (Pearson, 1901). PCA was conducted on the passive spectral data from ChemCam using the scikit-learn library in Python (Pedregosa et al., 2012). To understand the influence of compositional features on the dataset and subsequent major PCs, the PCs were plotted against each other, spectral parameters (as described in Section 3.2), and LIBS elemental abundances. Correlations were reported using Spearman's rank correlation coefficient, which describes how well the relationship between two variables can be expressed a monotonic function (Spearman, 1904). PCA has proved useful in capturing the variability of ChemCam LIBS spectra (Anderson et al., 2011) and also has been applied to analyses of planetary reflectance spectral datasets (Farrand et al., 2013). Loading plots show the wavelength contributions to each PC and were very helpful in interpreting the meaning of PC values. Positive loadings for a PC in a given wavelength region mean that higher reflectance in that range would lead to higher values for that PC; negative loadings for a PC in a given wavelength region mean that higher reflectance in that range would lead to lower values for that PC. The terms "contribute positively" and "contribute negatively" (to a given PC) are used to describe positive and negative loadings. The distance from zero indicates the relative influence at a given wavelength.

### 3.5 CheMin Data

The CheMin instrument uses X-ray diffraction to measure the presence and abundance of minerals and X-ray amorphous materials in drilled rock and scooped soil samples in Gale crater (Blake et al., 2012). CheMin observations were compared to ChemCam passive spectral parameters to see how ferric minerals affect the relative reflectance data. CheMin requires sample processing (i.e., drilling or scooping), and as a result there are far fewer observations compared to ChemCam. CheMin typically analyzes a sample drilled from a depth of 3-4 cm (Anderson et al., 2012), whereas ChemCam only probes a few micrometers below the surface per laser shot (Maurice et al., 2012). Analyses of CheMin data identify ~20-70% X-ray amorphous materials in every sample measured to date, and it is very difficult to characterize the identity of the amorphous material(s) from the XRD data alone (Rampe et al., 2020a). The amorphous component may have a substantial impact on the target's reflectance data because mass balance calculations of the amorphous component composition using CheMin and APXS data suggest the amorphous component is typically enriched in $FeO_T$, potentially corresponding to nanophase ferric oxides (e.g., Rampe et al., 2020a).

## 4. Results

### 4.1 Principal Component Analysis

The first principal component (PC1) accounted for 92.62% of the variance in the dataset and was strongly correlated with average relative reflectance (Spearman's $\rho = 0.99$; Fig. 3a). PC1's loadings were all positive and mirrored the average ChemCam reflectance spectrum, as expected (Fig. 4a). PC2 explained 6.61% of the variance and was negatively correlated with BD535 (Fig. 3b) and R6744 and positively correlated with R6084 ($\rho = -0.73$, -0.90, and 0.80 respectively). The wavelength range around 535 nm contributed positively to PC2 and wavelengths between 750 and 840 nm contributed negatively (Fig. 4a). PC3 was weakly correlated with BD600 (Fig. 3c, $\rho = 0.60$). Wavelengths 550 nm to 650 nm contributed negatively and 750 nm to 840 nm wavelengths contributed positively to PC3 (Fig. 4a). PC4 was negatively correlated with S7584 (Fig. 3d) and the spectral maximum ($\rho = -0.85$ and -0.72 respectively). The areas around 560 nm and past 800 nm contributed negatively to PC4, whereas the 600 nm to 725 nm region contributed positively (Fig. 4a). PC3 and PC4 explained 0.42% and 0.23% of the variance respectively. The loading plots for PC5 through PC8 show a significant increase in volatility below 500 nm and an increase in noise overall (Fig. 4b). Cumulatively explaining less than 0.12% of the variance of the passive spectral dataset, PCs past PC4 were not found to meaningfully relate to any spectral features in the dataset. Fig. 5 shows PC2 plotted against PC1 and PC4 plotted against PC3 – as expected the PCs are not correlated with one another. Fig. 6 shows representative ChemCam spectra for maximum and minimum values for PCs 1-4.

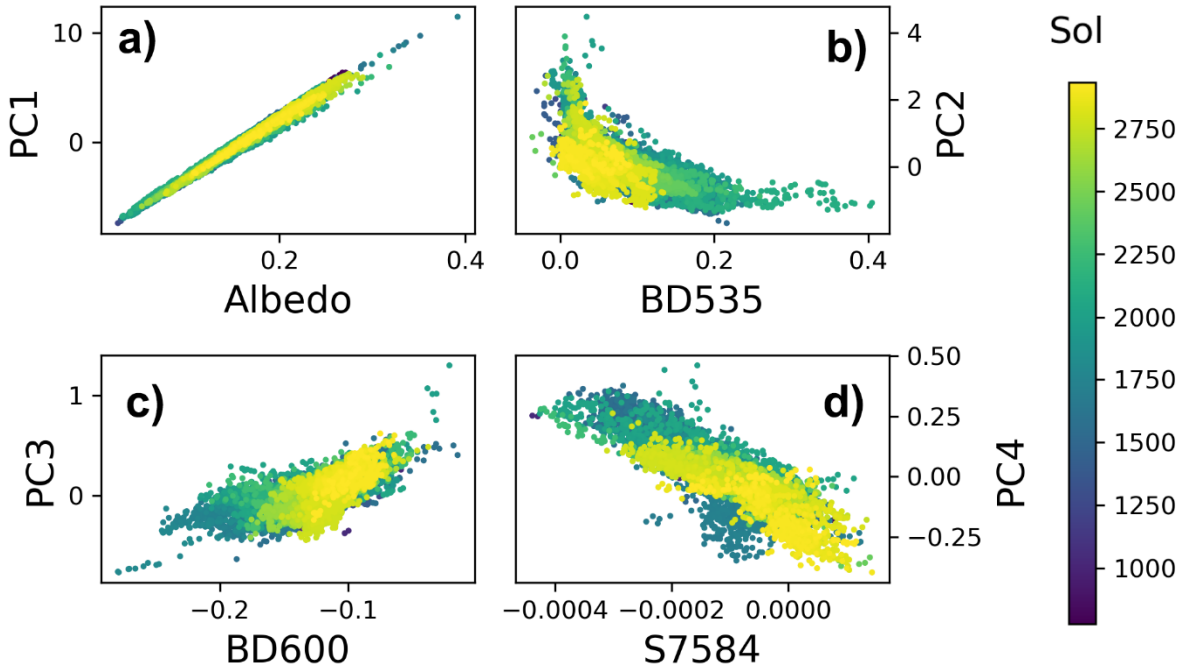


342 **Figure 3.** (a) PC1, (b) PC2, (c) PC3, and (d) PC4 plotted against spectral parameters. Negative
343 band depth values indicate the spectrum is concave at that wavelength. Colored by sol.

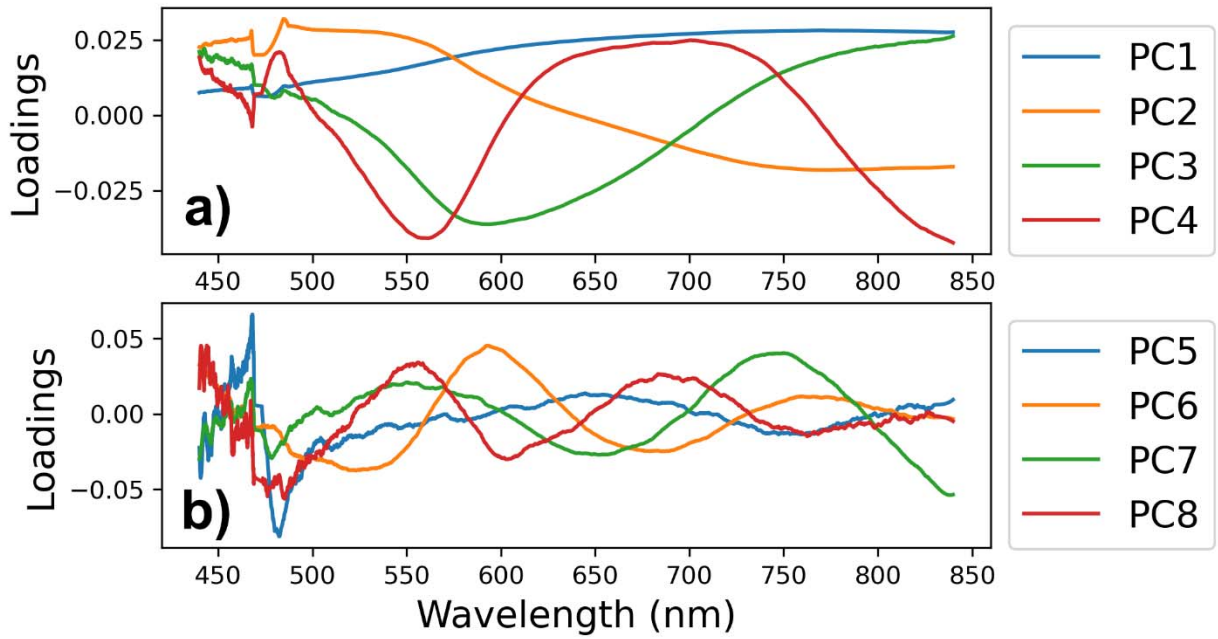


344 **Figure 4.** The PC loadings plotted against wavelength for (a) PCs 1-4 and (b) PCs 5-8. The
345 greater the loading value is above zero for a given wavelength and a given PC, the more that
346 wavelength range positively contributes to that PC. The more negative the loading is, the more
347 that wavelength range negatively contributes to that PC. A loading near zero indicates that region
348 is not important for that given PC.

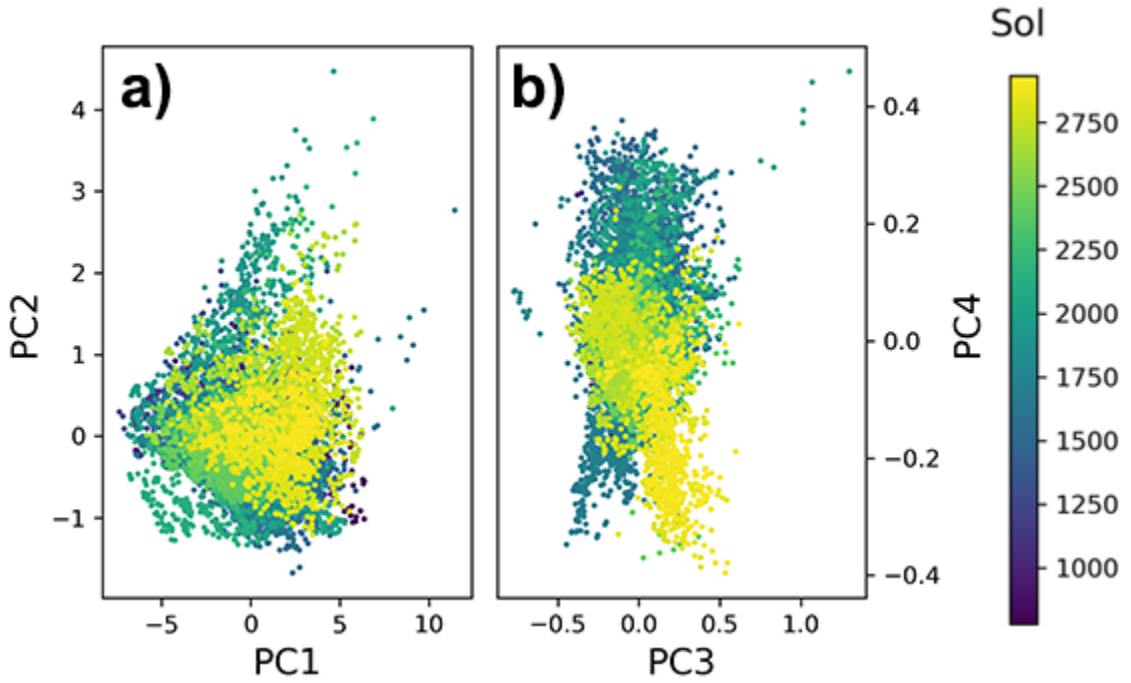


**Figure 5.** (a) PC2 plotted against PC1 and (b) PC4 plotted against PC3. Colored by sol number.

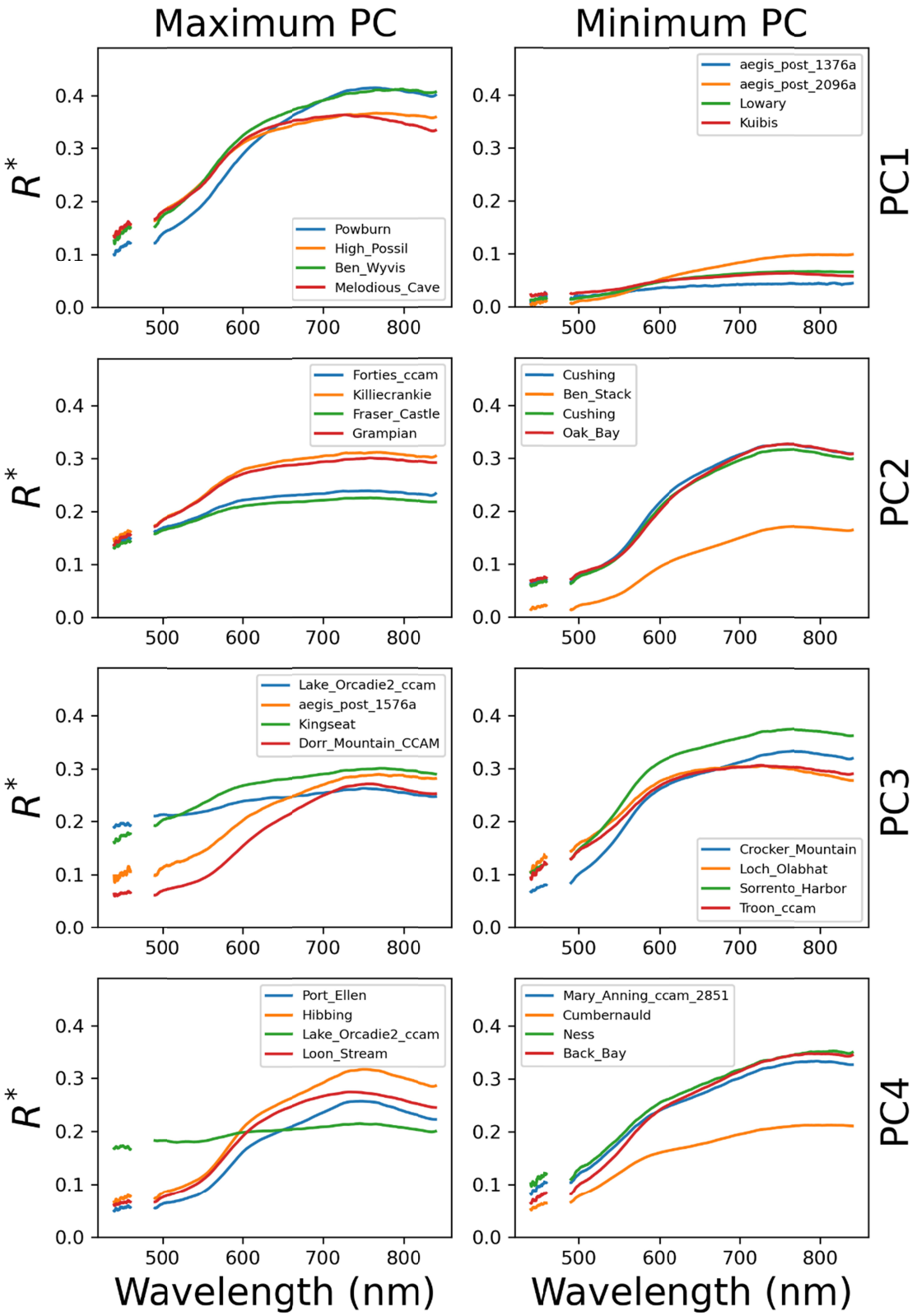


**Figure 6.** ChemCam passive spectra randomly chosen within the 150 observations with maximum (left) and minimum (right) values of PCs 1-4. Data near the VIO and NIR detector edges (460-490 nm) have low SNR and have been removed for visualization purposes.

### 4.2 Passive Spectral Parameters

There are variations in the calculated passive spectral parameters over Curiosity's traverse (Table 2), expanded here from previous work (e.g., Johnson et al., 2015, 2016; Fraeman et al., 2020). BD535 increases until the boundary between Sutton Island and Blunts Point (sol 1690) where it then decreases (Fig. 7c). This is mirrored by S7584, which broadly decreases until sol 1690 where it increases briefly (Fig. 7a), and it is also mirrored by the spectral maximum which peaks around sol 1690 (Fig. 7b). Another rapid decrease in BD535 is seen in Jura, followed by a more gradual decrease during the rest of the traverse. There is a small peak in BD535 near the area in the Vera Rubin ridge (VRR) with the deepest BD860 absorptions seen by CRISM from orbit (sol ~2004) (Fraeman et al., 2020). BD600, which is related to the strength of the short wavelength ferric oxide absorption edge (Morris et al., 1985; Johnson et al., 2015), largely stays between -0.05 and 0.15, except for the Jura member where it dips to as low as -0.28 (Fig. 7d). Negative band depth values indicate concavity in a spectrum, not an absorption. Many of the passive spectral parameters are correlated with each other (Table 3).

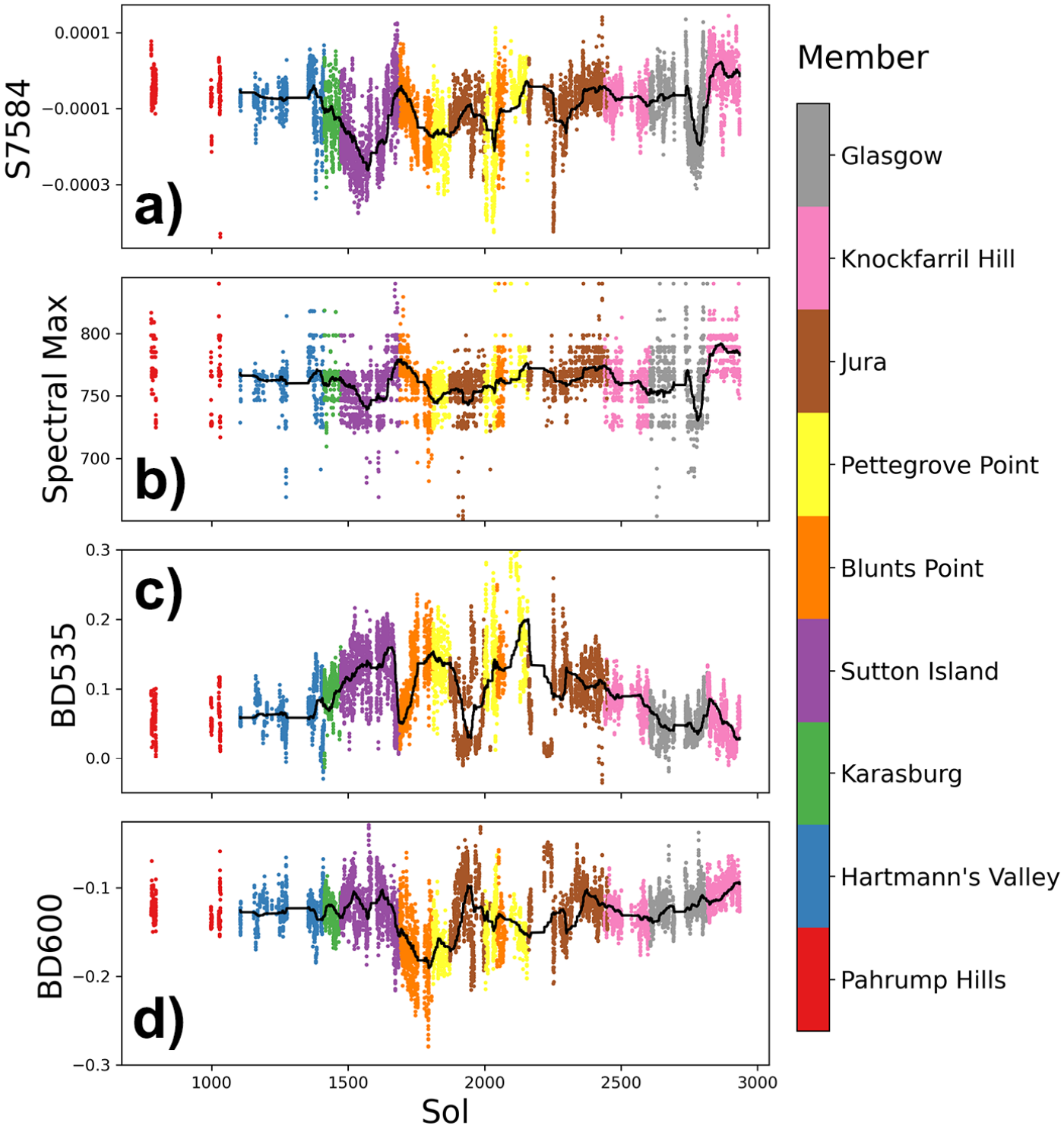


**Figure 7.** S7584 (a), Spectral maximum (b), BD535 (c), and BD600 (d) plotted against sol. Data are colored by geologic member. Running average of 250 observations (black line) is included.

**Table 3.** A Spearman's ρ Correlation Matrix of ChemCam Passive spectra

| | Sol | PC1 | PC2 | PC3 | PC4 | BD535 | BD600 | S7584 | R6744 | R6084 | Spectral Maximum | Avg. Relative Reflectance |
|---|---|---|---|---|---|---|---|---|---|---|---|---|
| **Sol** | 1.00 | 0.09 | 0.14 | 0.15 | -0.26 | -0.27 | 0.19 | 0.26 | 0.01 | -0.08 | 0.17 | 0.10 |
| **PC1** | 0.09 | 1.00 | -0.09 | -0.04 | 0.01 | -0.16 | 0.16 | -0.13 | 0.12 | -0.02 | 0.09 | 0.99 |
| **PC2** | 0.14 | -0.09 | 1.00 | -0.14 | -0.02 | -0.74 | 0.26 | 0.02 | -0.91 | 0.81 | -0.25 | 0.01 |
| **PC3** | 0.15 | -0.04 | -0.14 | 1.00 | 0.01 | 0.07 | 0.60 | 0.25 | -0.09 | -0.53 | 0.35 | -0.04 |
| **PC4** | -0.26 | 0.01 | -0.02 | 0.01 | 1.00 | 0.50 | 0.00 | -0.84 | -0.11 | 0.22 | -0.72 | 0.01 |
| **BD535** | -0.27 | -0.16 | -0.74 | 0.07 | 0.50 | 1.00 | -0.42 | -0.40 | 0.62 | -0.50 | -0.16 | -0.24 |
| **BD600** | 0.19 | 0.16 | 0.26 | 0.60 | 0.00 | -0.42 | 1.00 | 0.16 | -0.35 | -0.11 | 0.10 | 0.20 |
| **S7584** | 0.26 | -0.13 | 0.02 | 0.25 | -0.84 | -0.40 | 0.16 | 1.00 | 0.04 | -0.33 | 0.77 | -0.12 |
| **R6744** | 0.01 | 0.12 | -0.91 | -0.09 | -0.11 | 0.62 | -0.35 | 0.04 | 1.00 | -0.69 | 0.25 | 0.03 |
| **R6084** | -0.08 | -0.02 | 0.81 | -0.53 | 0.22 | -0.50 | -0.11 | -0.33 | -0.69 | 1.00 | -0.54 | 0.06 |
| **Spectral Maximum** | 0.17 | 0.09 | -0.25 | 0.35 | -0.72 | -0.16 | 0.10 | 0.77 | 0.25 | -0.54 | 1.00 | 0.06 |
| **Avg. Relative Reflectance** | 0.10 | 0.99 | 0.01 | -0.04 | 0.01 | -0.24 | 0.20 | -0.12 | 0.03 | 0.06 | 0.06 | 1.00 |

## 4.3 Spectral Endmembers

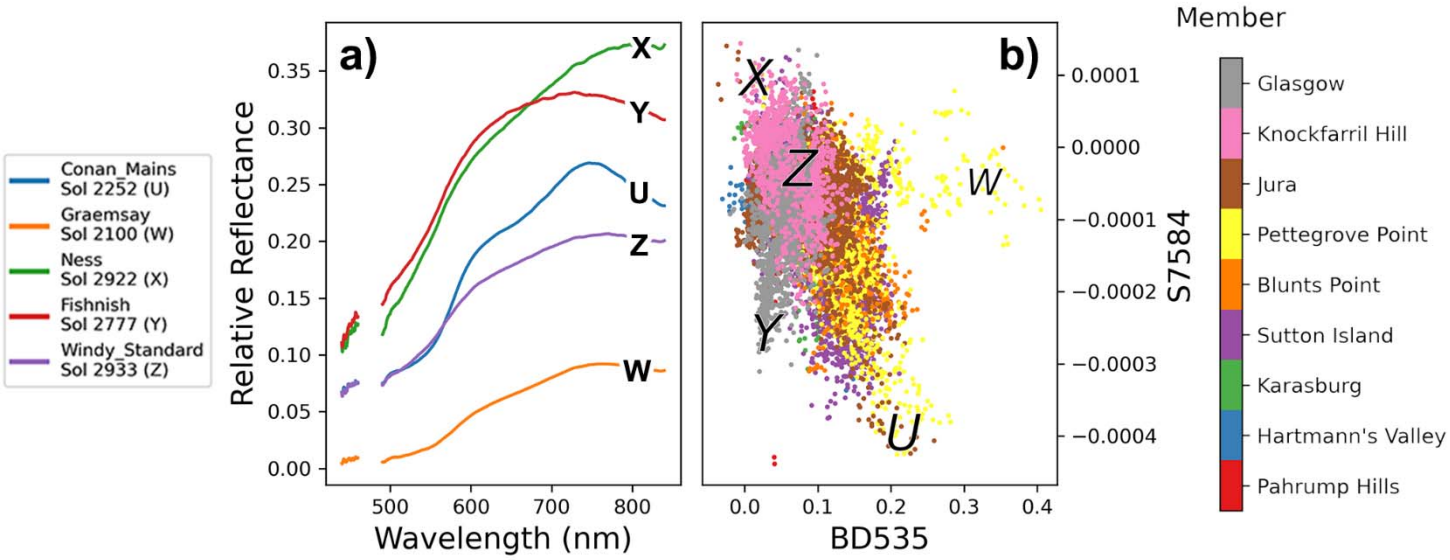


**Figure 8.** (a) Relative reflectance plotted against wavelength for five endmember spectra. (b) S7584 plotted against BD535, colored by geologic member, for all passive ChemCam observations in the dataset. Letters U-Z in (b) correspond to the spectra shown in (a), which are averages for a given target. Low SNR data around the VIO/NIR detector gap (~460-490 nm) have been removed.

Results from the above principal component analysis show focusing on trends in BD535 and S7584 is a good way to visualize spectral variability of the dataset. Plotting these two spectral

parameters on a scatter plot reveals five distinct classes of spectra. Combined large BD535 values and negative NIR slopes (S7584) are typical of ferric oxides (e.g. Fraeman et al., 2020); an example of a ChemCam target with these features ("Conan Mains", point U) is shown in Fig. 8. "Ness", Point X (Fig. 8), is a target with no near-infrared (NIR) slope and near-zero BD535. "Fishnish", Point Y (Fig. 8), is a target representative of many measurements from the Glasgow member that have large NIR slopes but weak to near-zero BD535. "Windy Standard" Point Z, (Fig. 8), is spectrally similar to the average Murray and Carolyn Shoemaker formation bedrock, with BD535 of ~0.08 and S7584 between 0 and -0.0001.

Some spectra were affected by a dust storm. "Graemsay", Point W (Fig. 8), is a target with very strong BD535, low average relative reflectance, and anomalously high R6744 and is characteristic of ChemCam passive spectral observations taken during the 2018 global dust storm. The dust storm significantly increased dust optical depth at 880 nm ($\tau$) as measured by the Mastcam instrument on Curiosity, reaching a maximum of $\tau$=8.5 around sol 2100 (Guzewich et al., 2019). This resulted in poorly calibrated ChemCam relative reflectance observations with unusually high atmospheric dust contamination, in particular low average relative reflectance, very high band depth at 535 nm, and a ratio of the reflectance at 670 nm to 440 nm between 10 and 30. There are 44 of these dust storm points representing 15 distinct targets between sol 2093 and 2130.

### 4.4 Passive spectra compared to LIBS data

Correlations between passive spectral properties and elemental abundances measured by LIBS were explored to search for additional insight into the sources of spectral variability and compositional trends in Mt. Sharp bedrock. Of particular interest was any relationship (or lack thereof) between spectral parameters and $FeO_{T,}$ since the VNIR spectral range is sensitive to charge-transfer and crystal-field absorptions most commonly associated with iron-bearing minerals. Correlations between spectral parameters and other elements could also highlight compositionally distinct regions.

When considering all Mt. Sharp group bedrock targets, no correlations between any of the major or trace oxides measured by LIBS and passive spectral features were found (Table 4). Ferric related spectral parameters such as PC2 and BD535 did not have any correlation with the iron oxide totals ($FeO_T$) from LIBS observations ($\rho$ = -0.03 and 0.17 respectively, Table 4) when viewed over the entire traverse, there were weak correlations in a subset of rock targets near the transition between the Sutton Island and Blunts Point stratigraphic members (Figure 9). There were also weak correlations ($\rho \approx -0.5$) between PC4 and high magnesium targets (Fig. 10a) in the Sutton Island-Blunts Point transition (~sol 1690), as well as in the Knockfarril Hill member. Examination of spectra of high MgO targets in both of these regions show they have weak BD535 and shallow S7584 (Point X, Fig. 8; Fig. 11). In these same two stratigraphic intervals, correlations between PC4 and high MnO targets were even more apparent (Fig. 10b). Targets that were examined around sol 1690 (near the Sutton Island – Blunts Point transition) have very low PC4 and high weight percent MnO, whereas the surrounding rocks have both much higher PC4 and low MnO values (Fig. 10b).

**Table 4.** A Spearman's ρ Correlation Matrix of ChemCam Passive and LIBS Data

| | Sol | PC1 | PC2 | PC3 | PC4 | BD535 | BD600 | S7584 | R6744 | R6084 | Spectral Maximum | Avg. Relative Reflectance |
|---|---|---|---|---|---|---|---|---|---|---|---|---|
| $FeO_T$ | -0.12 | -0.24 | -0.03 | -0.04 | 0.15 | 0.17 | -0.14 | -0.13 | -0.01 | 0.07 | -0.17 | -0.24 |
| MgO | 0.17 | -0.02 | -0.19 | 0.14 | -0.22 | -0.04 | 0.14 | 0.20 | 0.17 | -0.28 | 0.22 | -0.04 |
| $SiO_2$ | 0.23 | -0.01 | -0.11 | 0.16 | 0.06 | 0.09 | 0.13 | 0.07 | 0.12 | -0.20 | 0.04 | -0.02 |
| $K_2O$ | 0.15 | -0.16 | -0.05 | 0.12 | 0.15 | 0.18 | 0.04 | -0.04 | 0.03 | -0.09 | -0.08 | -0.16 |
| $Al_2O_3$ | -0.02 | 0.07 | -0.06 | -0.01 | 0.04 | 0.04 | 0.06 | 0.03 | 0.08 | -0.05 | 0.01 | 0.07 |
| CaO | -0.17 | 0.14 | 0.24 | -0.24 | -0.07 | -0.22 | -0.12 | 0.00 | -0.18 | 0.30 | -0.03 | 0.16 |
| $Na_2O$ | 0.00 | -0.03 | 0.10 | 0.03 | 0.02 | -0.06 | 0.10 | 0.07 | -0.08 | 0.06 | -0.03 | -0.02 |
| $TiO_2$ | 0.04 | -0.08 | 0.04 | 0.07 | 0.14 | 0.03 | 0.08 | -0.06 | -0.04 | 0.04 | -0.12 | -0.07 |
| MnO | -0.07 | 0.07 | 0.01 | -0.11 | -0.36 | -0.18 | -0.13 | 0.20 | 0.01 | 0.01 | 0.23 | 0.06 |

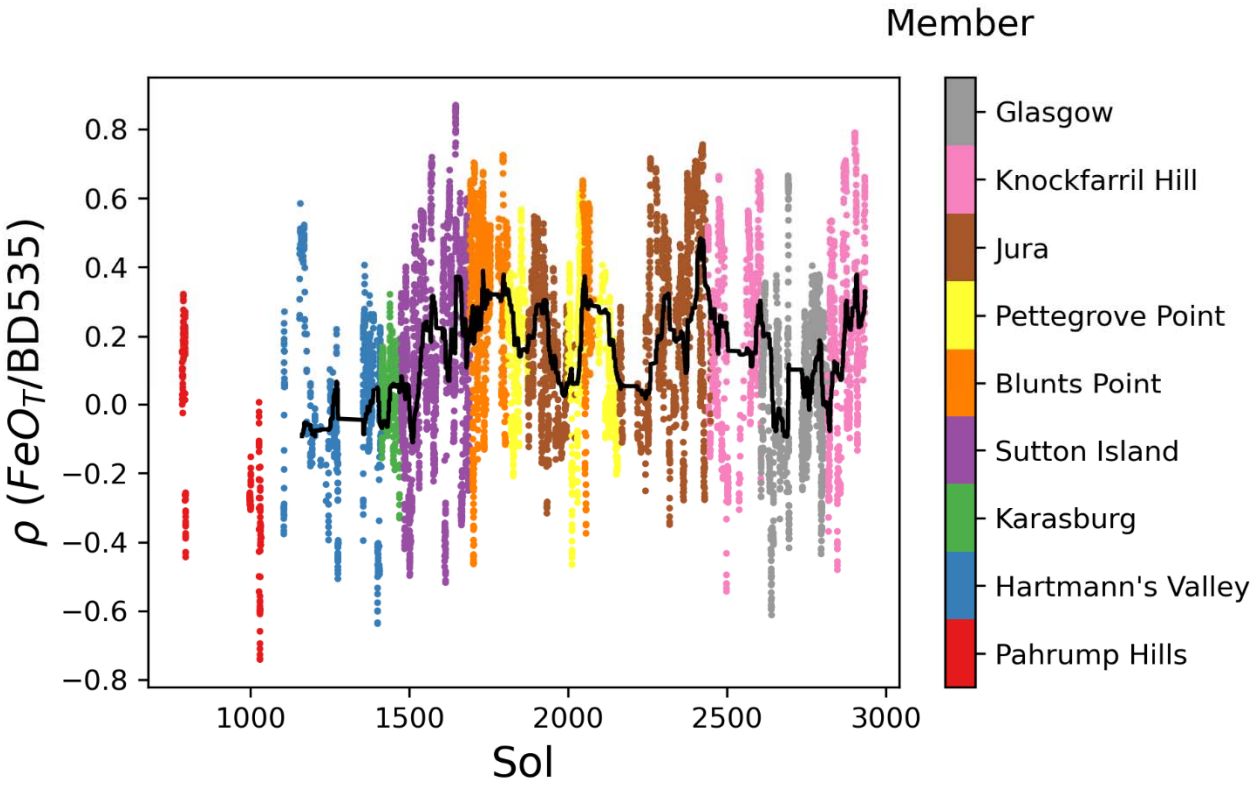


**Figure 9.** A rolling Spearman's correlation coefficient (ρ) of $FeO_T$ and BD535 with a window of 50 points. A rolling average of this data over 250 observations is plotted in black.

Although not evident in the bulk measurements, there is some relationship between PC4 and high magnesium targets (Fig. 10a). This is particularly obvious around the Sutton Island-Blunts Point transition (~sol 1690) and in Knockfarril Hill (an example spectrum is shown as point X in Fig. 8). This appears to stem from the fact that high MgO targets have shallow BD535 and little S7584 (Fig. 11). The same is true, and even more apparent, of high MnO targets. The sols immediately around sol 1690 have very low PC4 and weight percent MnO, whereas the surroundings have much higher PC4 and MnO values (Fig. 10b).

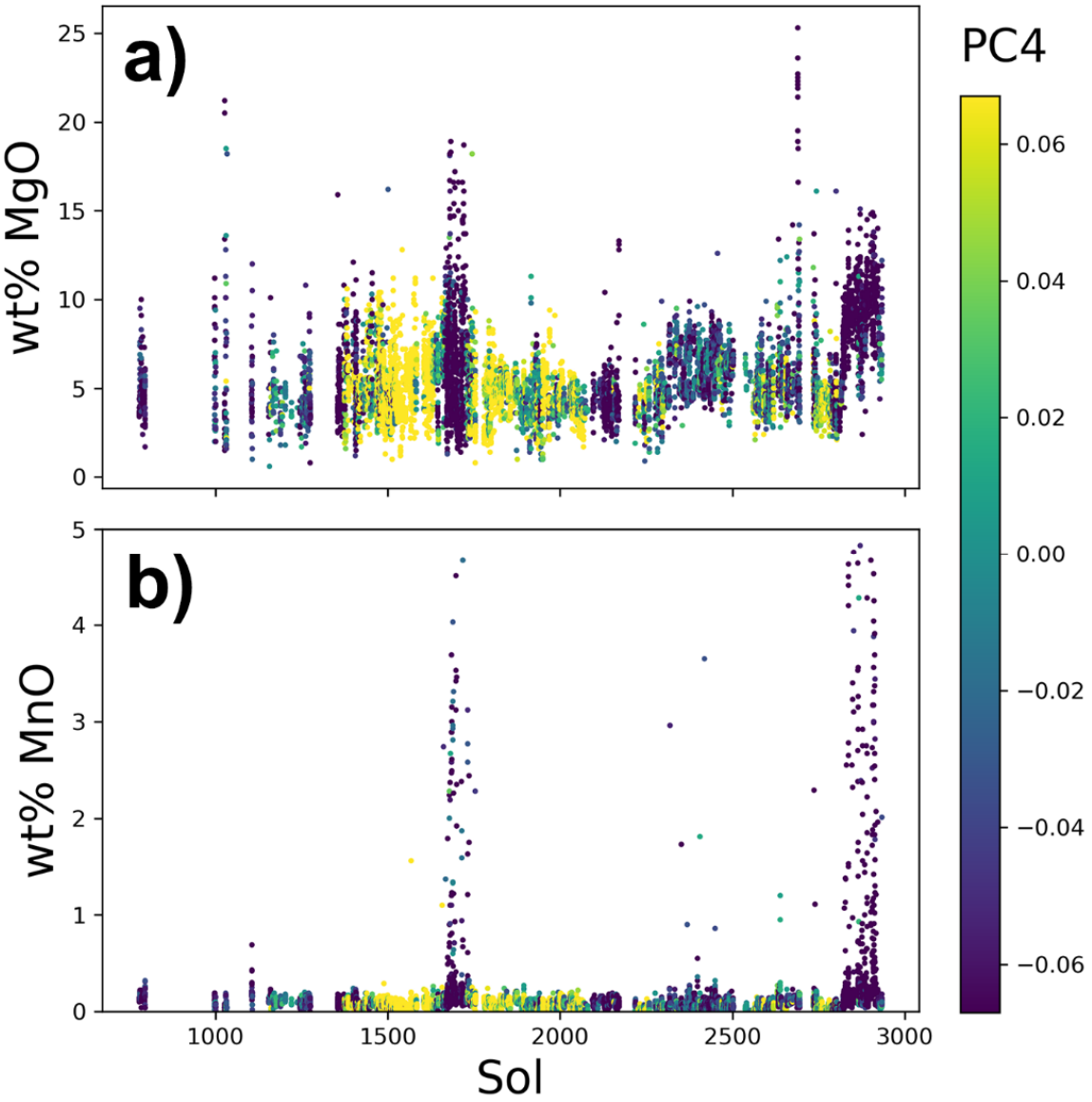


439 **Figure 10.** Weight percent MgO and MnO plotted against sol. Colored by PC4.

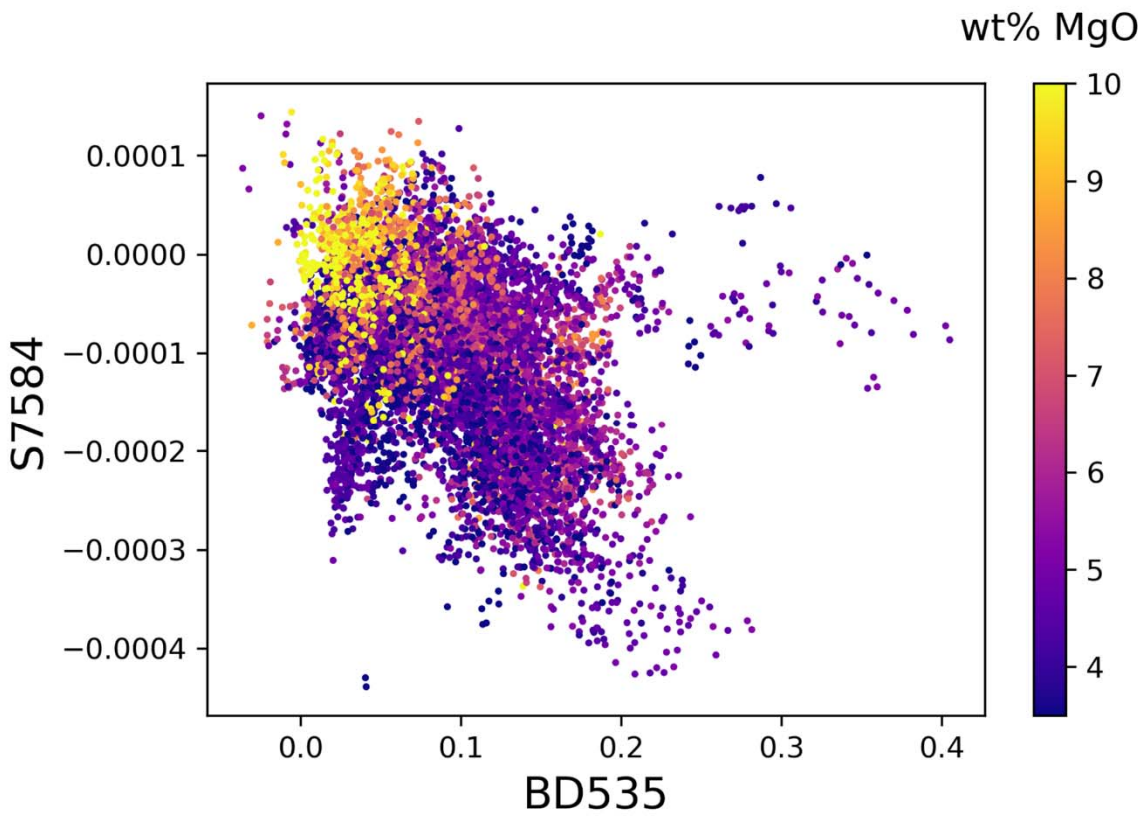


**Figure 11.** S7584 plotted against BD535. The points are colored by weight percent MgO, showing that high MgO correlates with low BD535 and high S7584. Outlying points at the right side of the plot near S7584 ~0 are due to poor calibration during the global dust storm.

Somewhat weaker correlations ($0.4 < \rho < 0.7$) between spectral parameters and LIBS chemistry when examined by individual stratigraphic member include:

- In Sutton Island, $SiO_2$ is negatively correlated with PC2 ($\rho = -0.44$) and MnO is correlated with PC4 ($\rho = -0.49$).
- In Blunts Point, all the major oxides are correlated with R6744 (and by extension PC2). R6744 is correlated with $FeO_T$, MgO, $SiO_2$, $K_2O$, $Al_2O_3$, CaO, $TiO_2$, and $Na_2O$ ($\rho = 0.52$, 0.41, 0.65, 0.63, 0.59, -0.60, 0.55, and 0.57 respectively). BD535 is correlated with $K_2O$ and MnO ($\rho = 0.44$ and -0.55 respectively). MnO and PC4 are also correlated ($\rho = -0.44$).
- In Knockfarril Hill, PC3 is correlated with MgO and MnO ($\rho = 0.58$ and 0.47 respectively). PC4 is correlated with $FeO_T$, MgO, $K_2O$, and MnO ($\rho = 0.49$, -0.70, 0.45, and -0.65 respectively). BD535 is correlated with $FeO_T$, MgO, $SiO_2$, $K_2O$, and MnO ($\rho =$ 0.40, -0.59, 0.45, 0.62, and -0.68 respectively).
- In Glasgow, S7584 is correlated with $K_2O$ and MnO ($\rho = -0.40$ and 0.50 respectively).

### 4.5 Comparison to CheMin Data

Although collected much more rarely than ChemCam LIBS data, co-located CheMin mineralogical data may provide additional insight into the source(s) of the spectral variability in the Mount Sharp group rocks. Wellington et al., (2017) found correlations between CheMin

analyses and Mastcam multispectral observations of drill tailings that suggested (1) the 800 nm spectral peak and 930 nm minimum in Yellowknife Bay (a Bradbury Group target) was derived from Fe-bearing phyllosilicates and pyroxenes, and (2) the 527 nm absorption in both Mastcam and ChemCam spectral data of Pahrump Hills target was consistent with the presence of crystalline hematite. Jacob et al., (2020) similarly examined CheMin data with coordinated Mastcam multispectral observations of drill tailings and hypothesized that variations in the 860 nm absorption feature were the result of a combination of variations in ferric phyllosilicate abundance, variations in clinopyroxene abundance, and the presence of red crystalline hematite.

14 targets measured by CheMin in the Murray or Carolyn Shoemaker formation over the sol range covered in this analysis have both passive and LIBS data collected before drilling (Table 5, 6).

Table 5 lists two spectral parameters from ChemCam passive data, BD535 and S7584 (Table 2), related to the presence of iron bearing minerals. 3 of these 14 targets were not brushed by the Dust Removal Tool (DRT). Even though the LIBS observations that are acquired before the passive spectra are often effective at clearing dust, the difference between DRT and non-DRT targets is still noted here due to possible differences in effectiveness of dust clearing between the two techniques. Dust can increase reflectance at longer wavelengths and can also reduce the depth of absorption features (Rice et al., 2022). Table 6 lists abundance of ferric materials inferred from CheMin data in these targets. Hematite and total ferric phase weight percent values in Table 6 are renormalized to 100% crystalline (i.e., without the amorphous components). Although there was evidence that many of the phyllosilicates in Gale crater also have some amount of $Fe^{3+}$, they contain variable amounts of $Fe^{2+}$ versus $Fe^{3+}$ in the octahedral sites, so were excluded in this comparison (Tu et al., 2021).

**Table 5.** Average BD535 and S7584 parameter values from ChemCam passive spectra for targets with both CheMin and ChemCam Data in the Murray and Carolyn Shoemaker Formations

| Drill Name | ChemCam Target Name | Sol | BD535 | S7584 ($10^{-4}$) |
|---|---|---|---|---|
| Marimba | Marimba | 1418 | 0.107 | -0.43 |
| Quela | Quela_DRT_ccam* | 1456 | 0.091 | -0.64 |
| Sebina | Sebina_ccam | 1492 | 0.125 | -1.95 |
| Duluth | Duluth_ccam | 2053 | 0.126 | -0.65 |
| Highfield | Rosebrae* | 2227 | 0.008 | -1.20 |
| Rock Hall | Rock_Hall_ccam_1 | 2257 | 0.114 | -1.62 |
| | Rock_Hall_ccam_2 | 2257 | 0.125 | -2.06 |
| | Rock_Hall_ccam_3 | 2257 | 0.115 | -2.04 |
| | Rock_Hall_ccam_4 | 2259 | 0.107 | -1.08 |
| Aberlady | Aberlady_ccam | 2367 | 0.089 | -0.71 |
| Kilmarie | Aberlady_ccam† | 2367 | 0.089 | -0.71 |
| Glen Etive 1 | Glen_Etive_1_ccam | 2482 | 0.097 | -0.72 |
| Hutton | Hutton_ccam | 2666 | 0.020 | -0.85 |
| | Hutton2_ccam | | 0.043 | -0.31 |

| | | | | |
|---|---|---|---|---|
| Glasgow | Glasgow_2_ccam*<br>Canongate* | 2753 | 0.071<br>0.040 | -0.49<br>-1.38 |
| Mary Anning | Mary_Anning_ccam | 2831 | 0.054 | 0.73 |
| Mary Anning 3 | Mary_Anning_3_ccam | 2869 | 0.03 | 0.26 |
| Groken | Groken_ccam | 2906 | 0.022 | 0.27 |

**Note.** Stoer was not included as it was in a period of high optical tau (the 2018 global dust storm).
*Quela, Highfield, and Glasgow did not have ChemCam data from a DRT surface.
†Aberlady_ccam was used for both the Aberlady and Kilmarie drills as they are very close to one another.

**Table 6.** CheMin data for targets in the Murray and Carolyn Shoemaker formation with both CheMin and ChemCam data

| **Drill Name** | **Crystalline Hematite (wt%)** | **Total Crystalline Ferric Phases (wt%)** | **$FeO_T$ in Amorphous Component (wt%)** | **Hematite Crystallite Size (nm)** |
|---|---|---|---|---|
| Marimba | 16.4 ± 2.1 | 17.9 ± 2.6 | 29.7 | 38.4 |
| Quela | 20.0 ± 1.5 | 21.4 ± 2.1 | 20.4 | 25.1 |
| Sebina | 20.4 ± 1.7 | 23.0 ± 2.3 | 18.8 | 26.8 |
| Duluth | 13.0 ± 0.8 | 13.0 ± 0.8 | 26.1 | 17.9 |
| Highfield | 20.2 ± 1.3 | 20.2 ± 1.3 | 7.4 | 30.7 |
| Rock Hall | 5.4 ± 0.4 | 21.0 ± 2.2 | 17.5 | 39.4 |
| Aberlady | 5.5 ± 1.4 | 5.5 ± 1.4 | 15.2 | 26.8 |
| Kilmarie | 3.8 ± 1.0 | 3.8 ± 1.0 | 12.4 | *No data* |
| Glen Etive 1 | 7.0 ± 2.5 | 7.0 ± 2.5 | 14.4 | 19.7 |
| Hutton | 4.8 ± 1.2 | 4.8 ± 1.2 | 8.4 | 28.1 |
| Glasgow | 13.4 ± 3.1 | 13.4 ± 3.1 | 12.3 | 16.2 |
| Mary Anning | 2.5 ± 1.6 | 2.5 ± 1.6 | 21.4 | 15.6 |
| Mary Anning 3 | 1.9 ± 0.5 | 1.9 ± 0.5 | 21.2 | 26.8 |
| Groken | 0.0 | 0.0 | 20.3 | 31.3 |

**Note.** Total crystalline ferric phases are CheMin-derived hematite, jarosite, and akaganeite abundances added together; magnetite is not included as it does not have ferric spectral expressions at 535 nm. CheMin abundances data were obtained from the Planetary Data System (Vaniman, 2022). $FeO_T$ in amorphous component is normalized to 100% amorphous. $FeO_T$ in amorphous component and hematite crystallite size were obtained from Achilles et al. (2020), Rampe et al. (2020), and Thorpe et al. (2022).

Highfield had a higher abundance of hematite than would be expected based on its weak 535 nm absorption and lack of downturn from 750-840 nm. This was interpreted to suggest that that hematite in that sample was coarse-grained "gray hematite" (Jacob et al., 2020; Rampe et al., 2020b). For sufficiently large hematite particles (>~3-5 μm), the ferric absorption edge is weak or not present, meaning it is approximately spectrally neutral over visible wavelengths, imparting a black to gray color (Catling & Moore, 2003; Lane et al., 2002; Morris et al., 2020). When

Highfield is not included, there was a strong correlation ($\rho = 0.75$) between BD535 and weight percent of total crystalline ferric phases as reported by CheMin (Fig. 12a, Table 7). This is consistent with findings from Mastcam multispectral data (Jacob et al., 2020; Rice et al., 2022; Wellington et al., 2017). S7584 was correlated with crystalline ferric phases ($\rho = -0.61$, Fig. 12b) and with weight percent amorphous $FeO_T$ ($\rho = 0.66$). The target with the highest average BD535 and steepest NIR slope (Sebina_ccam) corresponded to the sample with the most total crystalline ferric phases measured by CheMin (23 wt%). The target with the lowest weight percent ferric phases (Groken) was also the ChemCam target with the lowest average BD535 and very little S7584. Importantly, there were no targets with ChemCam-observed absorptions attributed to ferric iron that were not found to contain ferric phases as measured by CheMin. This indicates that the total abundance of crystalline ferric phases was a major source of variation in ChemCam passive reflectance spectra, with weight percent amorphous $FeO_T$ also playing a role. As demonstrated by Highfield, grain size of the ferric phases can also affect passive reflectance spectra.

**Table 7.** A Spearman's ρ Correlation Matrix of ChemCam Passive and Co-located CheMin Mineralogy Data

| | BD535 | S7584 | Hematite | Ferric Phases | Amorphous $FeO_T$ | Hematite size |
|---|---|---|---|---|---|---|
| **BD535** | 1 | -0.37 | 0.68 | 0.75 | 0.34 | -0.03 |
| **S7584** | -0.37 | 1 | -0.48 | -0.61 | 0.66 | -0.14 |
| **Hematite** | 0.68 | -0.48 | 1 | 0.92 | 0.08 | -0.16 |
| **Ferric Phases** | 0.75 | -0.61 | 0.92 | 1 | 0.04 | 0.07 |
| **Amorphous $FeO_T$** | 0.34 | 0.66 | 0.08 | 0.04 | 1 | -0.03 |
| **Hematite size** | -0.03 | -0.14 | -0.16 | 0.07 | -0.03 | 1 |

**Note.** Highfield was not included in this analysis.

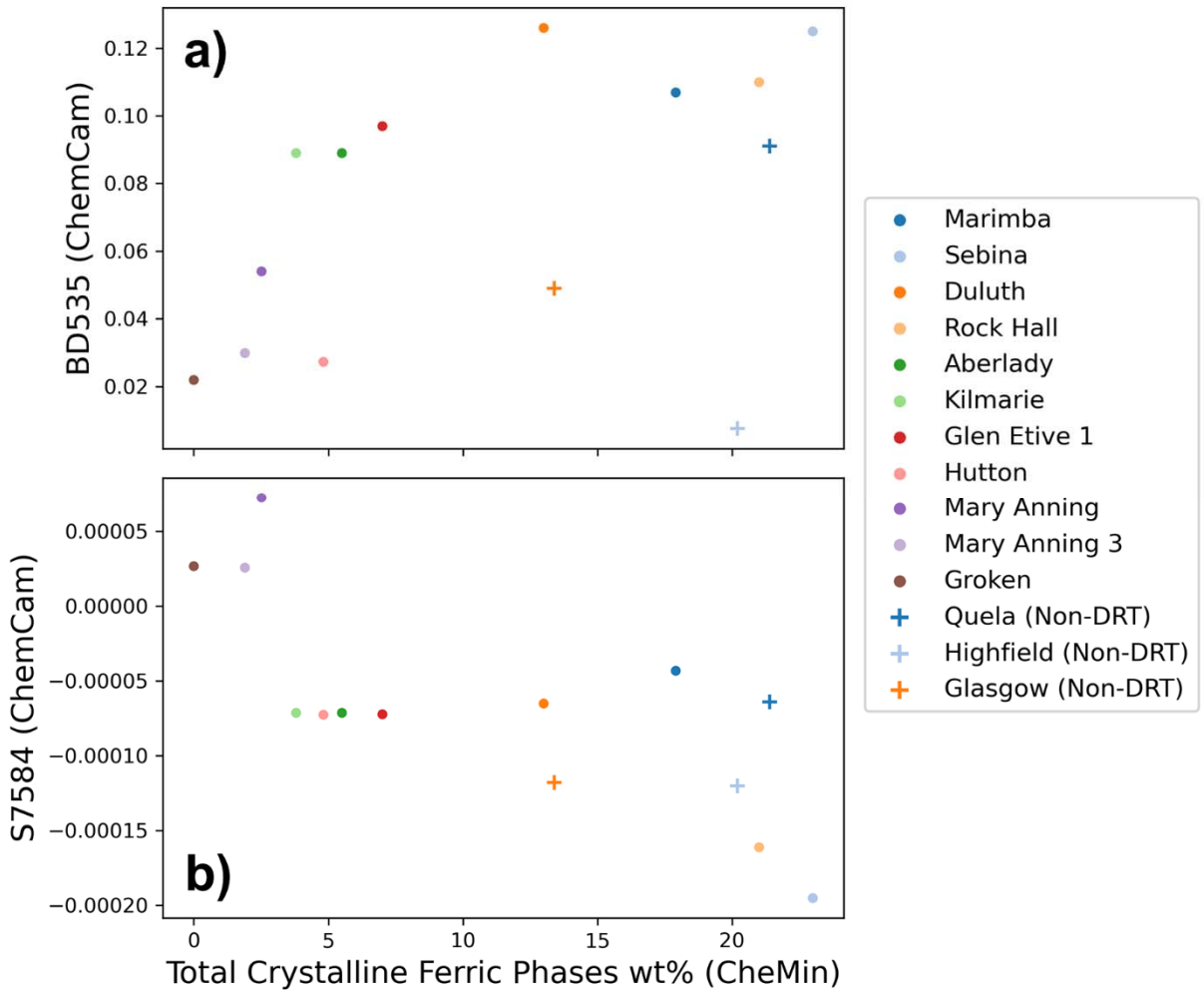


**Figure 12.** (a) BD535 and (b) S7584 derived from ChemCam passive observations vs. total crystalline ferric phases (hematite, jarosite, and akaganeite) from CheMin for all Mt. Sharp group drill holes for which a corresponding ChemCam observation. Targets marked with a cross represent observations not taken on a DRT surface.

## 5 Discussion

### 5.1 Summary of Spectral Variability in ChemCam Passive Spectra

PCA demonstrates that, after average relative reflectance, the biggest driver of variability in ChemCam passive spectra of Mt. Sharp group rocks are changes in ferric-related spectral absorptions. PC2 explains 6.61% of the variance of the dataset, and it is correlated with the depth of the 535 nm absorption ($Fe^{3+}$ electronic pair transition) (Fig. 3b), visible slope or "redness" (R6744), and near infrared slope (R6084). PC3, with 0.42% of the variance, is loosely correlated with BD600, which is related to the strength of the ferric oxide absorption edge (Fig. 3c), and PC4 (0.22% of the variance) is correlated with the slope from 750 nm and 840 nm, which is also related to electron transitions in ferric minerals (Fig. 3d). Loading plots for PCs 5-8 show a large increase in noise below 500 nm (Fig. 4b), and PCs 5-8 were not found to meaningfully relate to any spectral parameters.

Calculated passive spectral parameters varied significantly across the rover traverse. BD535 broadly increased until Pettegrove Point, near the VRR, where it decreased towards Glasgow and Knockfarril Hill. There was also a significant decrease in BD535 near sol 1690 which was mirrored by an increase in the NIR slope and the spectral maximum approaching 840 nm (see Section 5.3). A small peak in BD535 occurred near the area in the VRR with the strongest BD860 absorptions seen by CRISM from orbit (sol ~2004), although it was only moderately higher than other parts of the traverse (Fraeman et al., 2020).

The depth of the 535 nm absorption (~PC2) and S7584 (~PC4) cannot be used as a direct proxy for amount of iron oxides or ferric materials in a sample; factors such as mineral grain sizes and mineral mixtures also have also been shown to affect the strength of these features in Mt. Sharp group rocks (Jacob et al., 2020; Wellington et al. 2017). However, the 14 samples of Murray and Carolyn Shoemaker formation bedrock analyzed by CheMin that had corresponding ChemCam passive observations did show a correlation between strength of these absorption features and total ferric phases in the sample (Fig. 12), demonstrating abundance of ferric phases is an important driver in the presence and depth of these absorptions. The target with the highest abundance of ferric phases as measured by CheMin, Sebina, had a deep 535 nm absorption and strong NIR slope, while the target with the lowest abundance of ferric phases, Groken, had very little BD535 and flat NIR slopes (Fig. 12).

These findings are consistent with complementary Curiosity datasets. Spectral variations in Mastcam multispectral data are dominated by spectral differences that are attributed to hematite and other oxides (Rice et al., 2022; Jacob et al., 2020). Rice et al., (2022) identified nine distinct classes of Mastcam rock spectra from sols 0-2302, some of which are broadly similar to the ChemCam passive spectral endmembers identified in this work. For example, Class “U” (Fig. 8 and Fig. 13) is analogous to Class 4 (Hexriver) from Rice et al., (2022), both being consistent with red fine-grained hematite. Although a fewer number of samples were analyzed, CheMin analyses of drilled samples from the Murray formation varied in the amount and types of oxidized phases they contain (Bristow et al., 2018; Rampe et al., 2020a).

### 5.2 Spectrally unique areas

Figure 13 plots S7584 vs BD535 (correlated with PC4 and PC2 respectively), which reveals trends and spectrally unique regions in Mt. Sharp. Rocks in the Pettegrove Point member and portions of the Jura member associated with Vera Rubin ridge, have the highest combined BD535 and S7584 (class “U” in Fig. 8 and Fig. 13), as well as the lowest BD535 and S7584 (class “X”). The unique spectral properties in this area have been explored in detail (Fraeman et al., 2020; Horgan et al., 2020; Jacob et al., 2020; L’Haridon et al., 2020) and a leading hypothesis is hematite of variable grain sizes formed by diagenesis, possibly in association with the destruction of clay minerals by silica-poor brines (Bristow et al., 2021). Two other groups of spectrally distinct ChemCam passive observations include those taken in the Glasgow member and during the 2018 global dust storm. Each of these are discussed below.

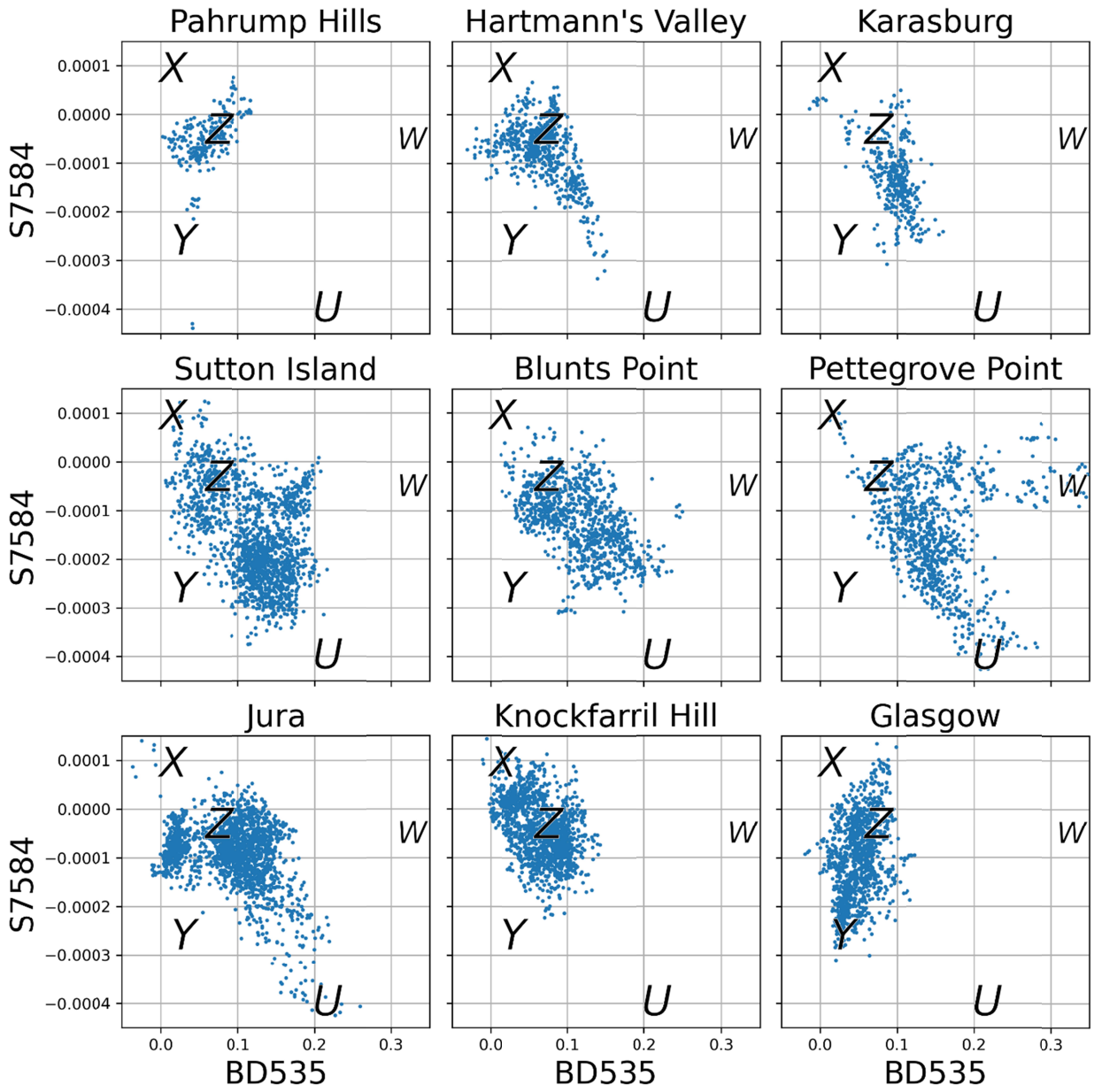


**Figure 13.** S7584 plotted against BD535 in each geologic member of the Mt. Sharp group. Spectral classes "U" through "Z" from Fig. 8 are also plotted for context.

### 5.2.1 Glasgow Member and the Hutton Interval

The transition between the Knockfarril Hill and Glasgow members is spectrally unique. Most Knockfarril Hill member targets have spectral features similar to average Mt. Sharp group bedrock (small BD535 and S7584 values), whereas many Glasgow targets have low BD535 and strongly negative NIR slopes (point Y in Fig. 8 and 13). The spectral difference could be the result of average Murray/Carolyn Shoemaker bedrock mixing with a new spectral endmember with less abundance or coarser grained ferric phases. Interestingly, analyses of sedimentary structures in this area showed a change in lithology that marked a significant transition from dominantly lacustrine to fluvial environments (Caravaca et al., 2022; Fedo et al., 2022). The concurrent changes in lithology and spectral properties could therefore be indicative of

compositional variations that either reflect that shift in primary depositional environment and/or different styles of diagenesis in this area.

A shift towards stronger S7584 but still shallow BD535 occurs around sol 2750-2800, at an area referred to as the Hutton interval. This interval occurs in the Glasgow member below the Siccar Point unconformity, and it is also associated with a color change in Mastcam color images, as well as a unique chemistry and mineralogy (Dehouck et al., 2022; Rudolph et al., 2022; Thompson et al., 2022; Thorpe et al., 2022). Specifically, the Hutton interval in the Glasgow member is characterized by a decrease in chemical index of alteration (CIA) values, localized enrichments and depletions in mobile elements, and significant amount of cristobalite and opal-CT (Dehouck et al., 2022; O'Connell-Cooper et al., 2022; Thorpe et al., 2022).

There are two endmember hypotheses to explain the unique composition of the Hutton interval: (1) there was a significant shift in the alteration conditions and/or nature of sediment source or (2) this interval is a region of enhanced diagenesis related to the Siccar Point unconformity (e.g. Dehouck et al., 2022). Each scenario predicts a different regional distribution of Hutton interval type material with respect to the Siccar Point unconformity, which Curiosity will have a chance to test to if it re-visits the unconformity at a higher elevation. If the Hutton interval is related to the diagenesis along the unconformity, rocks with similar compositional characteristics will re-appear. If the interval is related to depositional environments, the rocks near the Siccar Point unconformity to the south may be different. The discovery that the Hutton interval unconformity has unique spectral properties will provide additional criteria to test these hypotheses from Curiosity remote sensing data (whose acquisition is less resource intensive than drill sample collection for CheMin).

### 5.2.2 Targets acquired during high tau

ChemCam observations taken during the 2018 global dust storm were readily identified by their passive spectral features (class "W" in Fig. 8), in particular average relative reflectance below 0.085, BD535 above 0.3, and R6744 between 10 and 30. R6744 (the red-blue ratio) has been used as a first order approximation for dust cover at the Mars Pathfinder landing site (Johnson et al., 2003) and is similarly useful in ChemCam passive spectra. R6744 values above 10 occur exclusively during the 2018 dust storm between sol 2093 and 2130. We include dust storm observations here (44 measurements of 15 distinct targets) for completeness but note that spectral parameter correlations for these observations should be considered separately. This is evidenced by their very high BD535 but weak S7584 values (e.g., Fig 11), which are consistent with shadowed targets (Johnson et al., 2015).

## 5.3 Comparison between spectral and chemical properties of bedrock targets

Active LIBS chemical data collected from the same locations as passive spectral data provide a unique opportunity to directly compare chemical and spectral properties of Mt. Sharp bedrock.

Weight percent $FeO_T$ reported by LIBS and BD535 from passive spectra are not correlated (Spearman's $\rho = 0.18$) on the scale of Curiosity's traverse or generally within any individual member. The decoupled nature of $FeO_T$ and BD535 demonstrates that regions with strong 535 nm absorptions bands, like the Vera Rubin ridge, are not associated with areas where iron was added to the host bedrock (David et al., 2020), for example by being carried by anoxic

groundwater and subsequently precipitating at a redox interface (as proposed by Fraeman et al., 2013).

Interestingly, there was an increase in the correlation strength between $FeO_T$ and BD535 near the boundary of Sutton Island and Blunts Point and a small increase in Knockfarril Hill (Fig. 9) – two areas that are notable for their relatively high weight percent MnO targets (Fig. 10b). The presence of MnO is an indication of strongly oxidizing conditions (Lanza et al., 2016), but across the traverse there is no monotonic relationship between this potential signature of iron oxidation (the correlation coefficient of $FeO_T$ and BD535) and weight percent MnO.

The comparison of passive relative reflectance spectra and LIBS elemental data highlighted the boundary of Sutton Island and Blunts Point (sol 1690) as an area of interest. This region was proposed to be an interval of low lake level, as indicated by the presence of highly soluble hydrated magnesium sulfates associated with the bedrock detected both in-situ (Rapin et al., 2019) and from orbit (Sheppard et al., 2021). These magnesium sulfate rich bedrock targets were found to have significantly lower PC4 than the surrounding terrain (Fig. 10), corresponding to near zero S7584 (Fig. 7a), weak BD535 (Fig. 7c), and a spectral maximum approaching 800 nm (Fig 7b). This is consistent with Mastcam observations which suggest a significant decrease in crystalline hematite relative to the rest of the Murray formation and an increase in other iron bearing phases with band centers past the wavelength range of ChemCam (~910-930 nm) such as Fe/Mg smectite, jarosite, and akaganeite (Haber et al., 2022). This compositional change is indicative of more surface exposure and a low stand environment as described in Rapin et al., 2019. In clearly identifying this important region, principal component analysis of passive spectra has demonstrated that it is a valuable tool for gaining additional geochemical insight from ChemCam data.

In Blunts Point, PC2 and R6744 were moderately correlated with all major oxides reported by LIBS (R6744 had positive correlations with $FeO_T$, MgO, $SiO_2$, $K_2O$, $Al_2O_3$, $Na_2O$, and $TiO_2$ and negative correlations with CaO); (Section 4.4). This was not seen in any other stratigraphic member in this dataset and is likely the result of Ca sulfate cements that were previously identified in this region by ChemCam (Nellessen et al., 2019). Abundances of 10-25 wt% CaO consistent across a given target is characteristic of these cements (M. Nellessen et al., 2018). This is in contrast to vein observations (Fig. 2) showing pure Ca sulfates (e.g., lacking any silicate component and displaying higher Ca and S signatures). These cements are likely formed by Ca sulfate precipitation into the pore space prior to lithification of the sandstone. The cements thus indicate a change in depositional environment, such as a change in deposition rate, or more likely, a shoreline environment in which evaporation-dominated areas are separated from the main body of the lake (e.g., Rapin et al. 2019).

## 6 Conclusions

Passive relative reflectance spectra of bedrock targets taken by ChemCam in the Murray and Carolyn Shoemaker formations were analyzed using principal component analysis (PCA), spectral parameters, and compared to their corresponding LIBS elemental abundances. PCA of ChemCam passive spectra proved useful in highlighting geochemically distinct regions of the traverse. The Blunts Point-Sutton Island transition, which contains magnesium sulfate rich targets and has been proposed as an area of low lake level by Rapin et al. (2019), was found to

have zero 750 nm to 840 nm spectral slope (PC4) and weak 535 nm band depth (PC2), in agreement with Mastcam data from this interval (Haber et al., 2022). The Hutton interval (sol 2750-2800) was found to be spectrally distinct from the rest of the Mt. Sharp group, having strong 750 nm to 840 nm spectral slope slopes but little change in 535 nm band depth. This indicates either a change in alteration conditions or enhanced diagenesis in this region. Comparisons between spectral parameters and LIBS data in Blunts point also suggest influences from calcium cements. The correlation coefficient between $FeO_T$ reported by LIBS and BD535 from passive spectra was investigated as a tool for understanding changing oxidation conditions across Curiosity's traverse. Higher than average correlations between $FeO_T$ and BD535 were found in the Blunts Point-Sutton Island transition and Knockfarril Hill, regions known to be rich in MnO, but this signature of oxidizing conditions was not found to rise to significance on the scale of the traverse.

**Acknowledgements**

A portion of this research was carried out at the Jet Propulsion Laboratory, California Institute of Technology, under a contract with the National Aeronautics and Space Administration (80NM0018D0004). This work was funded by the JPL SURF Program, the NASA MSL Participating Scientist Program, and NASA's Mars Exploration Program support to the Mars Science Laboratory Mission. JF acknowledges the support from the Carlsberg Foundation. OG work on the ChemCam instrument supported by CNES.

**Data Availability Statement**

The MSL ChemCam Passive Surface Spectra bundle (Johnson, 2022) was obtained from the Planetary Data System (PDS). CheMin and LIBS data were also obtained from the PDS (Vaniman, 2022; Wiens, 2022). MSL Localizations for mapping were acquired on the PDS (Deen, 2015).

**References**

Achilles, C. N., Rampe, E. B., Downs, R. T., Bristow, T. F., Ming, D. W., Morris, R. V., et al. (2020). Evidence for Multiple Diagenetic Episodes in Ancient Fluvial-Lacustrine Sedimentary Rocks in Gale Crater, Mars. *Journal of Geophysical Research: Planets*, *125*(8). https://doi.org/10.1029/2019JE006295

Anderson, R. B., Morris, R. V., Clegg, S. M., Bell, J. F., Wiens, R. C., Humphries, S. D., et al. (2011). The influence of multivariate analysis methods and target grain size on the accuracy of remote quantitative chemical analysis of rocks using laser induced breakdown spectroscopy. *Icarus*, *215*(2), 608–627. https://doi.org/10.1016/j.icarus.2011.07.034

734 Anderson, R. C., Jandura, L., Okon, A. B., Sunshine, D., Roumeliotis, C., Beegle, L. W., et al.
735 (2012). Collecting Samples in Gale Crater, Mars; an Overview of the Mars Science
736 Laboratory Sample Acquisition, Sample Processing and Handling System. *Space Science*
737 *Reviews*, *170*(1–4), 57–75. https://doi.org/10.1007/s11214-012-9898-9
738 Bell, J. F. III McCord, T. B., & Owensby, P. D. (1990). Observational evidence of crystalline
739 iron oxides on Mars. *Journal of Geophysical Research*, *95*(B9), 14447.
740 https://doi.org/10.1029/JB095iB09p14447
741 Bell, J. F. III McSween, H. Y., Crisp, J. A., Morris, R. V., Murchie, S. L., Bridges, N. T., et al.
742 (2000). Mineralogic and compositional properties of Martian soil and dust: Results from
743 Mars Pathfinder. *Journal of Geophysical Research: Planets*, *105*(E1), 1721–1755.
744 https://doi.org/10.1029/1999JE001060
745 Bell, J. F. III, Godber, A., McNair, S., Caplinger, M. A., Maki, J. N., Lemmon, M. T., et al.
746 (2017). The Mars Science Laboratory *Curiosity* rover Mastcam instruments: Preflight and
747 in-flight calibration, validation, and data archiving. *Earth and Space Science*, *4*(7), 396–
748 452. https://doi.org/10.1002/2016EA000219
749 Bennett, K. A., Fox, V. K., Bryk, A., Dietrich, W., Fedo, C., Edgar, L., et al. (2022). The
750 Curiosity Rover's Exploration of Glen Torridon, Gale crater, Mars: An Overview of the
751 Campaign and Scientific Results. *Journal of Geophysical Research: Planets*.
752 https://doi.org/10.1029/2022JE007185
753 Blake, D., Vaniman, D., Achilles, C., Anderson, R., Bish, D., Bristow, T., et al. (2012).
754 Characterization and Calibration of the CheMin Mineralogical Instrument on Mars
755 Science Laboratory. *Space Science Reviews*, *170*(1–4), 341–399.
756 https://doi.org/10.1007/s11214-012-9905-1

Bristow, T. F., Grotzinger, J. P., Rampe, E. B., Cuadros, J., Chipera, S. J., Downs, G. W., et al. (2021). Brine-driven destruction of clay minerals in Gale crater, Mars. *Science*, *373*(6551), 198–204. https://doi.org/10.1126/science.abg5449

Bristow, T. F., Rampe, E. B., Achilles, C. N., Blake, D. F., Chipera, S. J., Craig, P., et al. (2018). Clay mineral diversity and abundance in sedimentary rocks of Gale crater, Mars. *Science Advances*, *4*(6), eaar3330. https://doi.org/10.1126/sciadv.aar3330

Calef III, F. J., & Parker, T. (2016). MSL Gale Merged Orthophoto Mosaic. PDS Annex, U.S. Geological Survey. Retrieved from http://bit.ly/MSL_Basemap

Caravaca, G., Mangold, N., Dehouck, E., Schieber, J., Zaugg, L., Bryk, A. B., et al. (2022). From Lake to River: Documenting an Environmental Transition across the Jura/Knockfarril Hill Members Boundary in the Glen Torridon Region of Gale crater (Mars). *Journal of Geophysical Research: Planets*. https://doi.org/10.1029/2021JE007093

Catling, D. C., and Moore, J. M. (2003). The nature of coarse-grained crystalline hematite and its implications for the early environment of Mars. *Icarus*, *165*(2), 277–300. https://doi.org/10.1016/S0019-1035(03)00173-8

Clegg, S. M., Wiens, R. C., Anderson, R., Forni, O., Frydenvang, J., Lasue, J., et al. (2017). Recalibration of the Mars Science Laboratory ChemCam instrument with an expanded geochemical database. *Spectrochimica Acta Part B: Atomic Spectroscopy*, *129*, 64–85. https://doi.org/10.1016/j.sab.2016.12.003

David, G., Cousin, A., Forni, O., Meslin, P. -Y., Dehouck, E., Mangold, N., et al. (2020). Analyses of High-Iron Sedimentary Bedrock and Diagenetic Features Observed With ChemCam at Vera Rubin Ridge, Gale Crater, Mars: Calibration and Characterization.

*Journal of Geophysical Research: Planets*, *125*(10). https://doi.org/10.1029/2019JE006314

Deen, R. (2015). MSL Mars Rover 6 RDR PLACES Rover Motion Counter V1.0 [Data set]. NASA Planetary Data System. https://doi.org/10.17189/1520397

Dehouck, E., Cousin, A., Mangold, N., Frydenvang, J., Gasnault, O., Forni, O., et al. (2022). Bedrock geochemistry and alteration history of the clay-bearing Glen Torridon region of Gale crater, Mars. *Journal of Geophysical Research: Planets*. https://doi.org/10.1029/2021JE007103

Edgar, L. A., Fedo, C. M., Gupta, S., Banham, S. G., Fraeman, A. A., Grotzinger, J. P., et al. (2020). A Lacustrine Paleoenvironment Recorded at Vera Rubin Ridge, Gale Crater: Overview of the Sedimentology and Stratigraphy Observed by the Mars Science Laboratory Curiosity Rover. *Journal of Geophysical Research: Planets*, *125*(3). https://doi.org/10.1029/2019JE006307

Farrand, W. H., Bell, J. F., Johnson, J. R., Rice, M. S., & Hurowitz, J. A. (2013). VNIR multispectral observations of rocks at Cape York, Endeavour crater, Mars by the Opportunity rover's Pancam. *Icarus*, *225*(1), 709–725. https://doi.org/10.1016/j.icarus.2013.04.014

Fedo, C. M., Bryk, A. B., Edgar, L. A., Bennett, K. A., Fox, V. K., Dietrich, W. E., et al. (2022). Geology and Stratigraphic Correlation of the Murray and Carolyn Shoemaker Formations Across the Glen Torridon Region, Gale Crater, Mars. *Journal of Geophysical Research: Planets*, *127*(9). https://doi.org/10.1029/2022JE007408

Fraeman, A. A., Arvidson, R. E., Catalano, J. G., Grotzinger, J. P., Morris, R. V., Murchie, S. L., et al. (2013). A hematite-bearing layer in Gale Crater, Mars: Mapping and implications

for past aqueous conditions. *Geology*, *41*(10), 1103–1106. https://doi.org/10.1130/G34613.1

Fraeman, A. A., Johnson, J. R., Arvidson, R. E., Rice, M. S., Wellington, D. F., Morris, R. V., et al. (2020). Synergistic Ground and Orbital Observations of Iron Oxides on Mt. Sharp and Vera Rubin Ridge. *Journal of Geophysical Research: Planets*, *125*(9). https://doi.org/10.1029/2019JE006294

Gasda, P. J., Anderson, R. B., Cousin, A., Forni, O., Clegg, S. M., Ollila, A., et al. (2021). Quantification of manganese for ChemCam Mars and laboratory spectra using a multivariate model. *Spectrochimica Acta Part B: Atomic Spectroscopy*, *181*, 106223. https://doi.org/10.1016/j.sab.2021.106223

Graff, T. G., Morris, R. V., Clegg, S. M., Wiens, R. C., & Anderson, R. B. (2011). Dust Removal on Mars using Laser-Induced Breakdown Spectroscopy, 1916. Presented at the 42nd Annual Lunar and Planetary Science Conference.

Guzewich, S. D., Lemmon, M., Smith, C. L., Martínez, G., de Vicente-Retortillo, Á., Newman, C. E., et al. (2019). Mars Science Laboratory Observations of the 2018/Mars Year 34 Global Dust Storm. *Geophysical Research Letters*, *46*(1), 71–79. https://doi.org/10.1029/2018GL080839

Gwizd, S., Fedo, C., Grotzinger, J., Banham, S., Rivera-Hernández, F., Stack, K. M., et al. (2022). Sedimentological and Geochemical Perspectives on a Marginal Lake Environment Recorded in the Hartmann's Valley and Karasburg Members of the Murray Formation, Gale Crater, Mars. *Journal of Geophysical Research: Planets*, *127*(8). https://doi.org/10.1029/2022JE007280

824 Haber, J. T., Horgan, B., Fraeman, A. A., Johnson, J. R., Bell, J. F., Rice, M. S., et al. (2022).
825 Mineralogy of a possible ancient lakeshore in the Sutton Island member of Mt. Sharp,
826 Gale crater, Mars, from Mastcam multispectral images. *Journal of Geophysical*
827 *Research: Planets*. https://doi.org/10.1029/2022JE007357
828 Horgan, B. H. N., Johnson, J. R., Fraeman, A. A., Rice, M. S., Seeger, C., Bell, J. F., et al.
829 (2020). Diagenesis of Vera Rubin Ridge, Gale Crater, Mars, From Mastcam
830 Multispectral Images. *Journal of Geophysical Research: Planets*, *125*(11).
831 https://doi.org/10.1029/2019JE006322
832 Izawa, M. R. M., Cloutis, E. A., Rhind, T., Mertzman, S. A., Applin, D. M., Stromberg, J. M.,
833 and Sherman, D. M. (2019). Spectral reflectance properties of magnetites: Implications
834 for remote sensing. *Icarus*, *319*, 525–539. https://doi.org/10.1016/j.icarus.2018.10.002
835 Jacob, S. R., Wellington, D. F., Bell, J. F., Achilles, C., Fraeman, A. A., Horgan, B., et al.
836 (2020). Spectral, Compositional, and Physical Properties of the Upper Murray Formation
837 and Vera Rubin Ridge, Gale Crater, Mars. *Journal of Geophysical Research: Planets*,
838 *125*(11). https://doi.org/10.1029/2019JE006290
839 Johnson, J. R. (2022). MSL ChemCam Passive Surface Spectra Bundle.
840 https://doi.org/10.17189/1520577
841 Johnson, J. R., Grundy, W. M., & Lemmon, M. T. (2003). Dust deposition at the Mars Pathfinder
842 landing site: observations and modeling of visible/near-infrared spectra. *Icarus*, *163*(2),
843 330–346. https://doi.org/10.1016/S0019-1035(03)00084-8
844 Johnson, J. R., Bell, J. F., Bender, S., Blaney, D., Cloutis, E., DeFlores, L., et al. (2015).
845 ChemCam passive reflectance spectroscopy of surface materials at the Curiosity landing
846 site, Mars. *Icarus*, *249*, 74–92. https://doi.org/10.1016/j.icarus.2014.02.028

Johnson, J. R., Bell, J. F., Bender, S., Blaney, D., Cloutis, E., Ehlmann, B., et al. (2016). Constraints on iron sulfate and iron oxide mineralogy from ChemCam visible/near-infrared reflectance spectroscopy of Mt. Sharp basal units, Gale Crater, Mars. *American Mineralogist*, *101*(7), 1501–1514. https://doi.org/10.2138/am-2016-5553

Lane, M. D., Morris, R. V., Mertzman, S. A., & Christensen, P. R. (2002). Evidence for platy hematite grains in Sinus Meridiani, Mars: PLATY HEMATITE GRAINS IN SINUS MERIDIANI, MARS. *Journal of Geophysical Research: Planets*, *107*(E12), 9-1-9–15. https://doi.org/10.1029/2001JE001832

Lanza, N. L., Clegg, S. M., Wiens, R. C., McInroy, R. E., Newsom, H. E., & Deans, M. D. (2012). Examining natural rock varnish and weathering rinds with laser-induced breakdown spectroscopy for application to ChemCam on Mars. *Appl. Opt.*, *51*(7), B74–B82. https://doi.org/10.1364/AO.51.000B74

Lanza, N. L., Wiens, R. C., Arvidson, R. E., Clark, B. C., Fischer, W. W., Gellert, R., et al. (2016). Oxidation of manganese in an ancient aquifer, Kimberley formation, Gale crater, Mars: Manganese Fracture Fills in Gale Crater. *Geophysical Research Letters*, *43*(14), 7398–7407. https://doi.org/10.1002/2016GL069109

L'Haridon, J., Mangold, N., Fraeman, A. A., Johnson, J. R., Cousin, A., Rapin, W., et al. (2020). Iron Mobility During Diagenesis at Vera Rubin Ridge, Gale Crater, Mars. *Journal of Geophysical Research: Planets*, *125*(11). https://doi.org/10.1029/2019JE006299

Malin, M. C., Ravine, M. A., Caplinger, M. A., Tony Ghaemi, F., Schaffner, J. A., Maki, J. N., et al. (2017). The Mars Science Laboratory (MSL) Mast cameras and Descent imager: Investigation and instrument descriptions. *Earth and Space Science*, *4*(8), 506–539. https://doi.org/10.1002/2016EA000252

Maurice, S., Wiens, R. C., Saccoccio, M., Barraclough, B., Gasnault, O., Forni, O., et al. (2012). The ChemCam Instrument Suite on the Mars Science Laboratory (MSL) Rover: Science Objectives and Mast Unit Description. *Space Science Reviews*, *170*(1–4), 95–166. https://doi.org/10.1007/s11214-012-9912-2

Morris, R. V., Rampe, E. B., Vaniman, D. T., Christoffersen, R., Yen, A. S., Morrison, S. M., et al. (2020). Hydrothermal Precipitation of Sanidine (Adularia) Having Full Al,Si Structural Disorder and Specular Hematite at Maunakea Volcano (Hawai'i) and at Gale Crater (Mars). *Journal of Geophysical Research: Planets*, *125*(9). https://doi.org/10.1029/2019JE006324

Morris, R. V., Lauer, H. V., Lawson, C. A., Gibson, E. K., Nace, G. A., & Stewart, C. (1985). Spectral and other physicochemical properties of submicron powders of hematite (α-$Fe_2O_3$), maghemite (γ-$Fe_2O_3$), magnetite ($Fe_3O_4$), goethite (α-FeOOH), and lepidocrocite (γ-FeOOH). *Journal of Geophysical Research*, *90*(B4), 3126. https://doi.org/10.1029/JB090iB04p03126

Nellessen, M., Baker, A. M., Newsom, H. E., Jackson, R., Williams, J., Clegg, S. M., et al. (2018). Distribution and Analysis of Calcium Sulfate Cemented Sandstones Along the Msl Traverse, Gale Crater, Mars, *2018*, P31F-3760. Presented at the AGU Fall Meeting Abstracts.

Nellessen, M. A., Baker, A. M., Newsom, H. E., Jackson, R. S., Williams, J., Nachon, M., et al. (2019). Distribution and Analysis of Calcium Sulfate-Cemented Sandstones Along the MSL Traverse, Gale Crater, Mars, 3031. Presented at the 50th Annual Lunar and Planetary Science Conference.

O'Connell-Cooper, C. D., Thompson, L. M., Spray, J. G., Berger, J. A., Gellert, R., McCraig, M., et al. (2022). Statistical Analysis of APXS-Derived Chemistry of the Clay-Bearing Glen Torridon Region and Mount Sharp Group, Gale Crater, Mars. *Journal of Geophysical Research: Planets*, *127*(9). https://doi.org/10.1029/2021JE007177

Pearson, K. (1901). LIII. *On lines and planes of closest fit to systems of points in space*. *The London, Edinburgh, and Dublin Philosophical Magazine and Journal of Science*, *2*(11), 559–572. https://doi.org/10.1080/14786440109462720

Pedregosa, F., Varoquaux, G., Gramfort, A., Michel, V., Thirion, B., Grisel, O., et al. (2012). Scikit-learn: Machine Learning in Python (Version 4). https://doi.org/10.48550/ARXIV.1201.0490

Pelkey, S., and Jakosky, B. (2002). Surficial Geologic Surveys of Gale Crater and Melas Chasma, Mars: Integration of Remote-Sensing Data. *Icarus*, *160*(2), 228–257. https://doi.org/10.1006/icar.2002.6978

Peret, L., Gasnault, O., Dingler, R., Langevin, Y., Bender, S., Blaney, D., et al. (2016). Restoration of the Autofocus capability of the ChemCam instrument onboard the Curiosity rover. In *SpaceOps 2016 Conference*. Daejeon, Korea: American Institute of Aeronautics and Astronautics. https://doi.org/10.2514/6.2016-2539

Rampe, E. B., Blake, D. F., Bristow, T. F., Ming, D. W., Vaniman, D. T., Morris, R. V., et al. (2020). Mineralogy and geochemistry of sedimentary rocks and eolian sediments in Gale crater, Mars: A review after six Earth years of exploration with Curiosity. *Geochemistry*, *80*(2), 125605. https://doi.org/10.1016/j.chemer.2020.125605

Rampe, E. B., Bristow, T. F., Morris, R. V., Morrison, S. M., Achilles, C. N., Ming, D. W., et al. (2020). Mineralogy of Vera Rubin Ridge From the Mars Science Laboratory CheMin

915 Instrument. *Journal of Geophysical Research: Planets*, *125*(9).
916 https://doi.org/10.1029/2019JE006306
917 Rapin, W., Ehlmann, B. L., Dromart, G., Schieber, J., Thomas, N. H., Fischer, W. W., et al.
918 (2019). An interval of high salinity in ancient Gale crater lake on Mars. *Nature*
919 *Geoscience*, *12*(11), 889–895. https://doi.org/10.1038/s41561-019-0458-8
920 Rice, M. S., Seeger, C., Bell, J., Calef, F., St. Clair, M., Eng, A., et al. (2022). Spectral Diversity
921 of Rocks and Soils in Mastcam Observations Along the Curiosity Rover's Traverse in
922 Gale Crater, Mars. *Journal of Geophysical Research: Planets*, *127*(8).
923 https://doi.org/10.1029/2021JE007134
924 Rudolph, A., Horgan, B., Johnson, J., Bennett, K., Haber, J., Bell, J. F., et al. (2022). The
925 distribution of clay minerals and their impact on diagenesis in Glen Torridon, Gale crater,
926 Mars. *Journal of Geophysical Research: Planets*. https://doi.org/10.1029/2021JE007098
927 Savitzky, A., & Golay, M. J. E. (1964). Smoothing and Differentiation of Data by Simplified
928 Least Squares Procedures. *Analytical Chemistry*, *36*(8), 1627–1639.
929 https://doi.org/10.1021/ac60214a047
930 Sheppard, R. Y., Milliken, R. E., Parente, M., & Itoh, Y. (2021). Updated Perspectives and
931 Hypotheses on the Mineralogy of Lower Mt. Sharp, Mars, as Seen From Orbit. *Journal of*
932 *Geophysical Research: Planets*, *126*(2). https://doi.org/10.1029/2020JE006372
933 Sherman, D. M. (1985). The electronic structures of Fe3+ coordination sites in iron oxides:
934 Applications to spectra, bonding, and magnetism. *Physics and Chemistry of Minerals*,
935 *12*(3), 161–175. https://doi.org/10.1007/BF00308210
936 Sherman, D. M. and Waite, T. D. (1985). Electronic spectra of Fe^3+ oxides and oxide
937 hydroxides in the near IR and near UV. *American Mineralogist*, *70*, 1262–1269.

Sherman, D. M., Burns, R. G., & Burns, V. M. (1982). Spectral characteristics of the iron oxides with application to the Martian bright region mineralogy. *Journal of Geophysical Research*, *87*(B12), 10169. https://doi.org/10.1029/JB087iB12p10169

Spearman, C. (1904). The Proof and Measurement of Association between Two Things. *The American Journal of Psychology*, *15*(1), 72. https://doi.org/10.2307/1412159

Stack, K. M., Cofield, S. M., Fraeman, A. A., & Edwards, C. S. (2016). Geologic Map of the MSL Curisoity Rover Extended Mission Traverse of Aeolis Mons, Gale Crater, Mars (p. 283395). Presented at the GSA Annual Meeting in Denver, Colorado, USA - 2016. https://doi.org/10.1130/abs/2016AM-283395

Stack, K. M., Grotzinger, J. P., Lamb, M. P., Gupta, S., Rubin, D. M., Kah, L. C., et al. (2019). Evidence for plunging river plume deposits in the Pahrump Hills member of the Murray formation, Gale crater, Mars. *Sedimentology*, *66*(5), 1768–1802. https://doi.org/10.1111/sed.12558

Thompson, L. M., Spray, J. G., O'Connell-Cooper, C., Berger, J. A., Yen, A., Gellert, R., et al. (2022). Alteration at the Base of the Siccar Point Unconformity and Further Evidence for an Alkaline Provenance at Gale Crater: Exploration of the Mount Sharp Group, Greenheugh Pediment Cap Rock Contact With APXS. *Journal of Geophysical Research: Planets*, *127*(11). https://doi.org/10.1029/2021JE007178

Thomson, B. J., Bridges, N. T., Milliken, R., Baldridge, A., Hook, S. J., Crowley, J. K., et al. (2011). Constraints on the origin and evolution of the layered mound in Gale Crater, Mars using Mars Reconnaissance Orbiter data. *Icarus*, *214*(2), 413–432. https://doi.org/10.1016/j.icarus.2011.05.002

960 Thorpe, M. T., Bristow, T. F., Rampe, E. B., Tosca, N. J., Grotzinger, J. P., Bennett, K. A., et al.
961 (2022). Mars Science Laboratory CheMin data from the Glen Torridon region and the
962 significance of lake-groundwater interactions in interpreting mineralogy and sedimentary
963 history. *Journal of Geophysical Research: Planets*.
964 https://doi.org/10.1029/2021JE007099
965 Tu, V. M., Rampe, E. B., Bristow, T. F., Thorpe, M. T., Clark, J. V., Castle, N., et al. (2021). A
966 Review of the Phyllosilicates in Gale Crater as Detected by the CheMin Instrument on
967 the Mars Science Laboratory, Curiosity Rover. *Minerals*, *11*(8), 847.
968 https://doi.org/10.3390/min11080847
969 Vaniman, D. (2022). MSL Mars Chemistry and Mineralogy 4 RDR V1.0 [Data set]. NASA
970 Planetary Data System. https://doi.org/10.17189/1519497
971 Vasavada, A. R. (2022). Mission Overview and Scientific Contributions from the Mars Science
972 Laboratory Curiosity Rover After Eight Years of Surface Operations. *Space Science*
973 *Reviews*, *218*(3), 14. https://doi.org/10.1007/s11214-022-00882-7
974 Viviano, C. E., Seelos, F. P., Murchie, S. L., Kahn, E. G., Seelos, K. D., Taylor, H. W., et al.
975 (2014). Revised CRISM spectral parameters and summary products based on the
976 currently detected mineral diversity on Mars. *Journal of Geophysical Research: Planets*,
977 *119*(6), 1403–1431. https://doi.org/10.1002/2014JE004627
978 Wellington, D. F., Bell, J. F., Johnson, J. R., Kinch, K. M., Rice, M. S., Godber, A., et al. (2017).
979 Visible to near-infrared MSL/Mastcam multispectral imaging: Initial results from select
980 high-interest science targets within Gale Crater, Mars. *American Mineralogist*, *102*(6),
981 1202–1217. https://doi.org/10.2138/am-2017-5760CCBY

Wiens, R.C. (2022). MSL Mars ChemCam LIBS Spectra 4/5 RDR V1.0 [Data set]. NASA Planetary Data System. https://doi.org/10.17189/1519485

Wiens, R. C., Maurice, S., Barraclough, B., Saccoccio, M., Barkley, W. C., Bell, J. F., et al. (2012). The ChemCam Instrument Suite on the Mars Science Laboratory (MSL) Rover: Body Unit and Combined System Tests. *Space Science Reviews*, *170*(1–4), 167–227. https://doi.org/10.1007/s11214-012-9902-4